sustainability

MDPI

Article

Unveiling the Potential of Strain-Engineered Zinc-Blende ZnTe for Solar Energy Conversion: First-Principles Insights into Structural Stability, Optoelectronic Properties, and Photocatalytic Performance

Abdellah Bouzaid [1,2], Younes Ziat [1,2,*], Youssef Jouad [1,2], Hamza Belkhanchi [1,2,*] and Mohammed Miri [1,2]

[1] Engineering and Applied Physics Laboratory (EAPL), Superior School of Technology, Sultan Moulay Slimane University, Beni Mellal 23000, Morocco
[2] The Moroccan Association of Sciences and Techniques for Sustainable Development (MASTSD), Beni Mellal 23000, Morocco
* Correspondence: ziat.younes@usms.ma (Y.Z.); hamzastudentestbm@gmail.com (H.B.)

Abstract

The escalating demand for clean energy and environmental remediation has intensified research into advanced photocatalytic and photovoltaic materials capable of harvesting solar energy efficiently, thereby supporting renewable energy technologies and the transition toward a low-carbon future. Among these materials, zinc-blende (ZB) ZnTe is a promising II–VI semiconductor owing to its direct band gap of approximately 2.291 eV. However, its relatively wide band gap limits its ability to harness a broader portion of the solar spectrum. In this study, first-principles calculations were performed using the WIEN2k package and the Tran–Blaha modified Becke–Johnson (TB-mBJ) potential to systematically investigate the effects of isotropic tensile strain (0–5%) on the structural, mechanical, dynamical, electronic, optical, photovoltaic, and photocatalytic properties of ZnTe. The stability of ZB ZnTe was evaluated using formation energy calculations, elastic constant analysis, and phonon dispersion analysis, confirming its thermodynamic, mechanical, and dynamical stability across the studied strain range. All strained structures retain a direct band gap, which decreases progressively from 2.291 eV in the unstrained state to 1.712 eV at 5% tensile strain, demonstrating effective modulation of the electronic structure through strain engineering. This reduction is accompanied by enhanced optical absorption and optical conductivity in the visible region, indicating improved light-harvesting potential. Consequently, the photovoltaic performance, assessed using the spectroscopic limited maximum efficiency (SLME) model, improved substantially, with the SLME increasing from 16.71% in the unstrained structure to 28.83% at 5% tensile strain. Under acidic conditions, the band-edge positions meet the thermodynamic requirements for overall water splitting and CO_2 reduction throughout the investigated strain range, while the theoretical solar-to-hydrogen (STH) efficiency increases from 7.09% in the unstrained structure to 12.08% at 5% tensile strain. This improvement is accompanied by a narrowing of the pH range suitable for photocatalytic reactions. Regarding pollutant degradation, the thermodynamic favorability of $\bullet O_2^-$ generation is maintained at all strain levels, whereas •OH generation becomes unfavorable under tensile strain, indicating that $\bullet O_2^-$ is likely to be the predominant reactive oxygen species. Although the limited availability of •OH may constrain the complete mineralization of recalcitrant organic pollutants, further oxidation through alternative reaction pathways may still enable their conversion into CO_2, H_2O, and inorganic ions. This study establishes tensile strain engineering as a theoretical strategy for tailoring the optoelectronic properties of ZnTe for photovoltaic and multifunctional photocatalytic ap-

Check for updates

Academic Editors: Samuele Memme, Mattia Parenti and Marco Fossa

Received: 18 September 2026
Revised: 24 October 2026
Accepted: 30 October 2026
Published: 3 November 2026

Copyright: © 2026 by the authors. Licensee MDPI, Basel, Switzerland. This article is an open access article distributed under the terms and conditions of the Creative Commons Attribution (CC BY) license.

plications, providing insights into its potential for advancing next-generation solar energy conversion and environmental remediation technologies.

Keywords: ZnTe; tensile strain engineering; density functional theory; sustainable solar energy conversion; optoelectronic properties; photocatalytic water splitting; CO_2 reduction; renewable energy; environmental remediation

1. Introduction

The growing demand for energy worldwide, along with the environmental impacts resulting from the heavy reliance on fossil fuels, has become one of the most pressing challenges confronting contemporary society [1–4]. The continuous depletion of non-renewable energy resources and the escalating emissions of greenhouse gases have intensified the need for sustainable and environmentally friendly energy solutions. Solar energy is especially attractive among renewable sources due to its abundance, inexhaustibility, and minimal environmental impact [5–8]. As a result, the development of highly efficient and durable solar energy conversion technologies has emerged as a major research priority for meeting future energy demands while promoting environmental sustainability [9]. Semiconductor (SC)-based photocatalysis has attracted considerable attention as a promising solar energy conversion technology because it enables the direct utilization of sunlight to drive a variety of redox reactions. Photocatalytic (PC) water splitting for hydrogen production offers a sustainable route toward clean fuel generation [10–13], while photocatalytic CO_2 reduction provides an attractive strategy for converting greenhouse gases into value-added chemicals and fuels [14–17]. Furthermore, PC degradation of organic pollutants has been widely explored for wastewater purification and environmental remediation [18–20]. The domain of semiconductor photocatalysis commenced with the groundbreaking research of Fujishima and Honda in 1972, who exhibited the photoelectrochemical dissociation of water utilizing TiO_2 as a SC photoelectrode [21]. Despite TiO_2's remarkable chemical stability, affordability, and potent oxidation capacity, its large band gap limits light absorption predominantly to the UV spectrum, including merely a little portion of the solar spectrum [22]. This limitation has prompted extensive research into alternative semiconductor materials capable of efficiently harvesting visible light while retaining appropriate electronic structures for photocatalytic reactions. To improve PC performance in SC materials, strategies such as elemental doping [23], pressure [24,25], and strain engineering [26–28] are employed. Pressure and strain engineering are particularly interesting as they modify electronic and optical properties without altering chemical composition. These methods can adjust the band gap, enhance visible-light absorption, improve charge-carrier separation, and optimize band-edge positions to boost PC activity. For instance, applying tensile strain to $CsInBr_3$ diminishes its band gap, augments visible-light absorption, and promotes the separation of photogenerated charge carriers, resulting in improved photocatalytic water-splitting efficacy [29]. Furthermore, the strained material demonstrates appropriate band-edge locations for CO_2 reduction and retains effective PC activity across an extensive pH range [29]. Likewise, strain engineering has been shown to augment the PC characteristics of WSe_2 by reducing its band gap, enhancing visible-light absorption, and facilitating charge-carrier movement, thus improving its efficacy for H_2 production [30]. Furthermore, ZnTe is a well-known II-VI SC with a cubic zinc-blende crystal structure and a direct band gap of around 2.26 eV [31–34], making it a promising material for a variety of optoelectronic applications [35–38]. Furthermore, II-VI SCs, particularly CdX and ZnX (X = S, Se, and

Te), have received a lot of attention due to their advantageous electronic structures, great optical properties, and high potential for photocatalytic applications [39–42].

Recent studies have further demonstrated the relevance of these materials for solar-energy conversion and optoelectronic technologies. Venkatesh et al. [43] investigated ZnTe/Cu back-contact engineering in CdTe solar cells, reporting a power conversion efficiency of 16.8% for the optimized configuration. Suchikova et al. [44] examined CdxTeyOz/CdS/ZnO heterostructures, highlighting the importance of phase composition and interfacial properties, while Lamonova et al. [45] explored the luminescence behavior of Fe- and Cr-co-doped ZnSe single crystals, demonstrating the influence of dopants and defect-related effects on their optical properties.

Strain engineering has emerged as a promising strategy for tailoring the electronic and optical properties of semiconductors. Previous theoretical investigations of two-dimensional ZnTe have shown that compressive strain modifies the bandgap magnitude, whereas tensile strain can induce an indirect-to-direct bandgap transition, accompanied by changes in the optical response [46]. Although these findings demonstrate the sensitivity of ZnTe to lattice deformation, they concern a two-dimensional system and cannot be directly extrapolated to bulk zinc-blende ZnTe. Furthermore, the extent to which isotropic tensile strain affects the structural stability, optoelectronic properties, and photovoltaic performance of bulk ZnTe remains insufficiently understood within a unified theoretical framework. Its potential for photocatalytic applications, including hydrogen production via water splitting, CO_2 reduction, and organic-pollutant degradation, also warrants systematic assessment. In particular, the interplay between strain-induced changes in the material properties and its suitability for these applications has not been comprehensively established. These limitations motivate a systematic investigation of strained bulk ZnTe that considers both its stability and its potential for solar-energy conversion and environmental remediation.

To address these research gaps, the present study employs first-principles density functional theory (DFT) calculations to systematically investigate the structural, elastic, and dynamical stability, as well as the electronic, optical, photovoltaic, and photocatalytic properties of bulk zinc-blende ZnTe under isotropic tensile strain ranging from 0% to 5%. The results demonstrate that ZnTe maintains mechanical and dynamical stability throughout the investigated strain range, while its thermodynamic stability is assessed based on the calculated formation energies. Furthermore, tensile strain reduces the band gap and modifies the optical response, leading to enhanced absorption in the visible-light region. The photocatalytic potential of strained ZnTe is also examined for hydrogen production via water splitting, CO_2 reduction, and organic-pollutant degradation by evaluating the relevant thermodynamic criteria. This comprehensive investigation elucidates the influence of isotropic tensile strain on the stability and functional properties of bulk ZnTe and provides theoretical insights into its potential applications in photovoltaic energy conversion, solar-driven fuel production, CO_2 conversion, and environmental remediation.

2. Computational Methodologies

The electronic structure computations were conducted using DFT and the FP-LAPW method, as implemented in the WIEN2k software (Version 23.2) [47]. The exchange-correlation potential for structural optimization was addressed using the PBE-GGA [48]. The conventional PBE-GGA functional is known to underestimate the band gap energies of SCs due to its approximate description of the exchange-correlation potential. To enhance the accuracy of electronic structure calculations, particularly for band gap energy, the TB-mBJ potential was utilized [49–51]. This method produces band gap values that are in good agreement with existing experimental results [31–34]. The electronic structure calculations were considered self-consistent when the total energy and charge convergence thresholds reached 10^{-5} Ry and

10^{-4} e, respectively. The Brillouin zone was sampled using a 10 × 10 × 10 Monkhorst–Pack k-point grid, resulting in approximately 1000 k-points being utilized throughout the entire Brillouin zone. The FP-LAPW basis set was defined by the parameter $R_{MT} \times K_{MAX} = 7$, where R_{MT} denotes the smallest muffin-tin radius, and K_{MAX} specifies the maximum reciprocal lattice vector used in the plane-wave expansion of the interstitial region. Additionally, the elastic constants were calculated using the IRelast package within WIEN2k, employing a k-point mesh of approximately 10,000 k-points in the Brillouin zone [52]. The Phonopy package has been utilized to estimate phonon modes based on force constants [53]. Furthermore, Figure 1 depicts the optimized crystal structures of the investigated materials as visualized using the VESTA software (Version 3) [54].

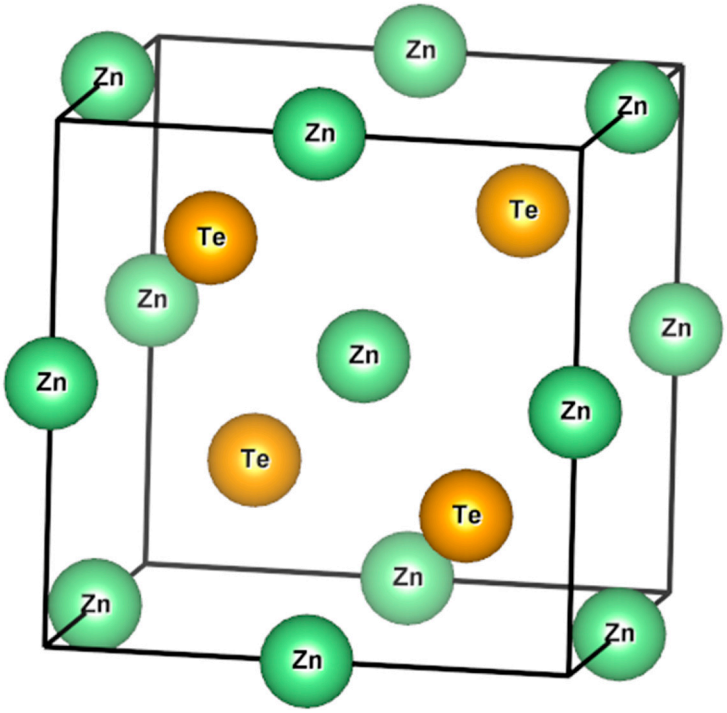


Figure 1. Crystal structure of zinc-blende ZnTe.

To investigate the structural response of ZnTe under hydrostatic (isotropic) tensile strain, the strain was systematically increased from 0% to 5% in increments of 1%. The strain was applied by uniformly expanding all three lattice parameters, thereby preserving the cubic symmetry of the crystal. The isotropic tensile strain was defined as follows [55]:

$$\text{Strain}(\%) = \frac{a - a_0}{a_0} \times 100\% \quad (1)$$

where a_0 denotes the equilibrium lattice parameter, whereas a signifies the lattice parameter under strain.

3. Results and Discussion

3.1. Structural Stability

The optimized crystal structure of ZnTe, obtained using the GGA framework, is illustrated in Figure 1. ZnTe crystallizes in the cubic zinc-blende phase, which has the space group F-43m. This structure consists of two interpenetrating face-centered cubic (FCC) sublattices: one sublattice is occupied by Zn atoms, while the other is occupied by Te atoms. Zn atoms have coordinates (0, 0, 0), (0, 0.5, 0.5), (0.5, 0, 0.5), and (0.5, 0.5, 0), while Te atoms have coordinates (0.25, 0.25, 0.25), (0.25, 0.75, 0.75), (0.75, 0.25, 0.75), and

(0.75, 0.75, 0.25) [32]. The equilibrium structural parameters were obtained by fitting the computed total energy as a function of unit-cell volume to the Murnaghan equation of state [56], as seen in Figure 2a. The energy volume curves clearly show parabolic minima, indicating that the cubic phase in ZnTe is stable. The optimized lattice parameter for the ZnTe unit cell was found to be $a_0 = b_0 = c_0 = 6.1785$ Å, which is consistent with previous theoretical [32,57–59] and experimental results [32]. Additionally, Figure 2b shows that the lattice parameter increases continuously from 6.1785 Å in the unstrained structure (0% strain) to 6.490 Å under a 5% tensile strain. This trend indicates a gradual expansion of the crystal lattice in response to tensile deformation and confirms the anticipated structural response to the applied strain.

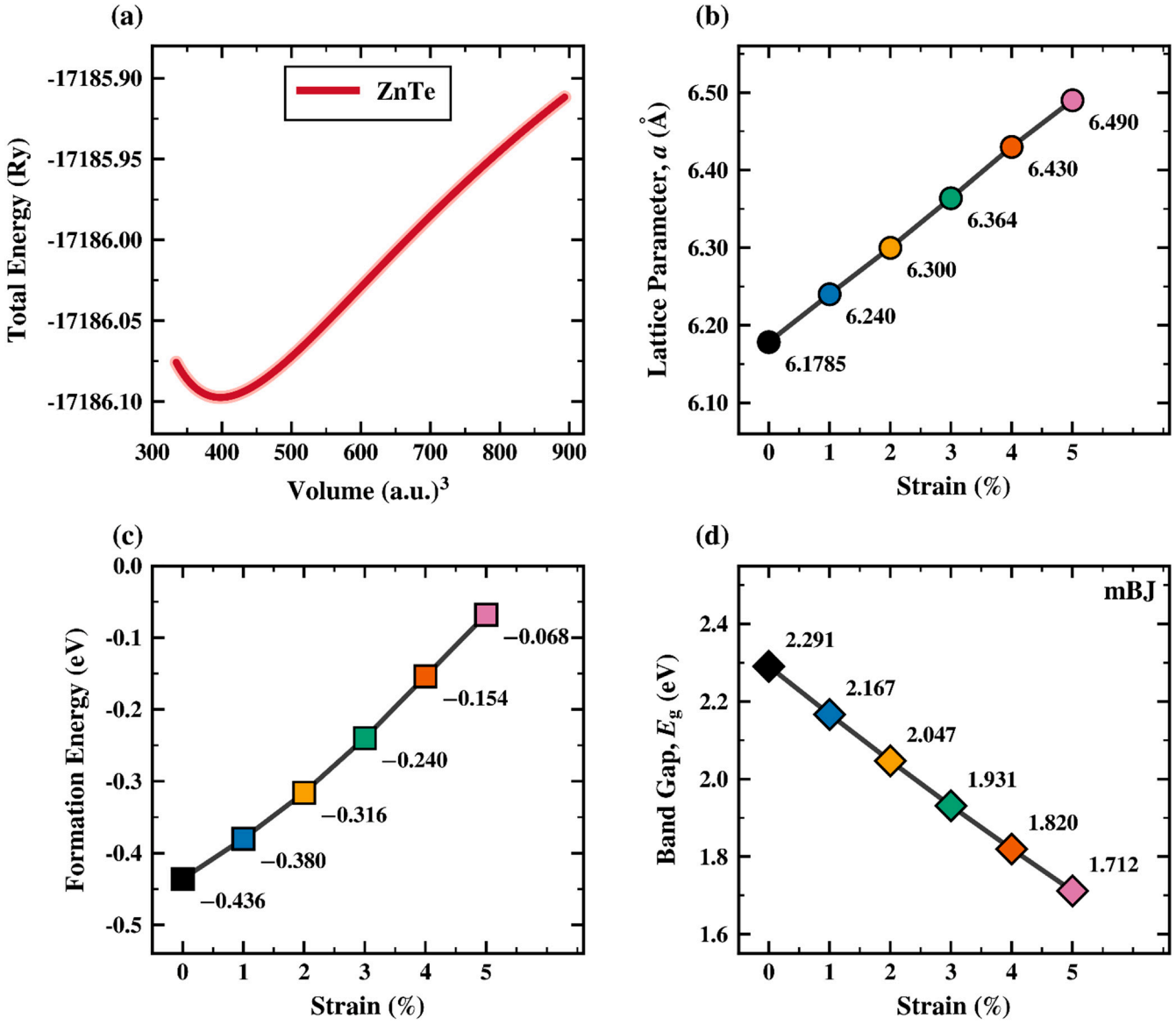


Figure 2. (**a**) Total energy as a function of unit-cell volume, (**b**) lattice parameter (Å), (**c**) formation energy (eV), and (**d**) band gap energy (eV) of ZnTe under tensile strain.

The thermodynamic stability of ZnTe under tensile strains (0–5%) was evaluated using calculated formation energies (E_f) to gain a better understanding of its structural stability. The E_f was obtained using Equation (2) [57], and the results are displayed in Figure 2b.

$$E_f = E_{ZnTe} - (E_{Zn} + E_{Te}) \quad (2)$$

where E_{ZnTe} signifies the total energy of the optimized ZnTe unit cell subjected to tensile stresses within 0 and 5%, whereas E_{Zn} and E_{Te} denote the total energies per atom of Zn and Te in their respective stable bulk reference phases.

The thermodynamic stability criterion commonly used in the literature states that a negative formation energy signifies that a compound is energetically favorable compared to its constituent elements [6]. As illustrated in Figure 2c, the calculated formation energy remains negative throughout the investigated range of tensile strain (0–5%). It increases from −0.436 eV at 0% strain to −0.068 eV at 5% strain. These results indicate that the compound remains energetically favorable relative to its constituent elements across the entire range of applied tensile strain.

To better clarify the mechanical response of ZnTe under strain, its elastic constants and mechanical properties were analyzed under isotropic tensile strain ranging from 0% to 5%, offering insights into its stability and resistance to deformation. The mechanical stability of the cubic crystal structure was assessed using the Born stability criteria, which define specific conditions based on the elastic constants. In this context, the independent elastic constants of the cubic system (C_{11}, C_{12}, and C_{44}) were calculated, and the results are presented in Table 1. The conditions required for mechanical stability are outlined in Equation (3) [60–62].

$$C_{11} - C_{12} > 0; C_{11} + 2C_{12} > 0; C_{11} > 0; C_{44} > 0 \quad (3)$$

Table 1. Computed elastic constants and mechanical parameters of ZnTe as a function of applied tensile strain.

	0%	1%	2%	3%	4%	5%
C_{11} (GPa)	66.3560	59.4697	55.0448	51.9180	47.0773	42.3109
C_{12} (GPa)	35.1866	29.5592	25.4159	21.5150	17.2027	13.3652
C_{44} (GPa)	42.9363	37.3218	33.4472	30.0241	25.8173	22.4561
Cp (GPa)	−7.7497	−7.7626	−8.0313	−8.5091	−8.6146	−9.0909
B (GPa)	45.5764	39.5294	35.2922	31.6493	27.1609	23.0138
G (GPa)	28.6112	25.8636	24.1231	22.8473	20.7289	18.8299
E (GPa)	70.9807	63.6984	58.9403	55.2477	49.5750	44.3845
ν	0.2404	0.2314	0.2217	0.2091	0.1958	0.1786
B/G	1.5930	1.5284	1.4630	1.3853	1.3103	1.2222
μ_M	1.0615	1.0592	1.0552	1.0541	1.0520	1.0248
A	2.7550	2.4956	2.2577	1.9751	1.7284	1.5516

The strain dependence of the elastic constants reflects the progressive softening of the ZnTe lattice under isotropic tensile deformation. In particular, the quantity $C_{11} + 2C_{12}$ decreases with increasing strain, indicating a reduced resistance to volume-changing deformation. Based on the elastic constants reported in Table 1, the values of $C_{11} - C_{12}$, $C_{11} + 2C_{12}$, and C_{44} remain positive throughout the investigated strain range. Therefore, the calculated structures satisfy the Born mechanical stability criteria for cubic crystals at all considered strain levels. This elastic softening is consistent with the reduction in characteristic phonon frequencies discussed in Section 3.2.

As reported in Table 1, the calculated elastic constants satisfy all the Born stability criteria under the investigated isotropic tensile-strain conditions, confirming the mechanical stability of the studied material. The calculated elastic constants decrease monotonically

with increasing isotropic tensile strain, indicating progressive elastic softening of the crystal. C_{11} decreases from 66.3560 GPa in the unstrained structure to 42.3109 GPa at 5% strain, while C_{12} and C_{44} decrease from 35.1866 to 13.3652 GPa and from 42.9363 to 22.4561 GPa, respectively. The more pronounced decrease in C_{12} indicates its greater sensitivity to isotropic tensile deformation, whereas the reduction in C_{44} reflects a weakening of the resistance to shear deformation. The decrease in C_{11} also reveals a reduction in longitudinal stiffness. Despite this strain-induced softening, the elastic constants continue to satisfy the Born stability criteria throughout the investigated strain range, confirming the mechanical stability of the cubic structure under isotropic tensile strain. The Cauchy pressure, defined as $C_p = C_{12} - C_{44}$, serves as a valuable qualitative indicator of the mechanical behavior of crystalline solids. Generally, positive Cauchy pressure is linked to ductile behavior, while negative values are typically indicative of brittleness [63]. The calculated results show that all the materials examined exhibit negative Cauchy pressure values, suggesting a primarily brittle mechanical response.

To assess the mechanical properties of ZnTe under applied tensile strain, we determined several important parameters: the bulk modulus (B), shear modulus (G), Young's modulus (E), Poisson's ratio (ν), Pugh's ratio (B/G), and the machinability index (μ_M). These parameters were calculated from the elastic constants using the Voigt–Reuss–Hill (VRH) approximation [64]. They characterize the elastic stiffness and resistance to deformation of ZnTe, providing valuable insights into its ductile-brittle behavior and machinability. The calculations were based on established relationships reported in the literature [65–67].

$$B = B_R = B_V = \frac{1}{3}(C_{11} + 2C_{12}) \quad (4)$$

$$G_V = \frac{1}{5}(C_{11} - C_{12} + 3C_{44}) \quad (5)$$

$$G_R = \frac{5C_{44}(C_{11} - C_{12})}{4C_{44} + 3(C_{11} - C_{12})} \quad (6)$$

$$B = \frac{1}{2}(B_V + B_R) \quad (7)$$

$$G = \frac{1}{2}(G_V + G_R) \quad (8)$$

$$E = \frac{9BG}{3B + G} \quad (9)$$

$$\nu = \frac{3B - 2G}{2(3B + G)} \quad (10)$$

The calculated mechanical properties of the investigated material under isotropic tensile strain ranging from 0% to 5% are summarized in Table 1. The B, G, and E decrease monotonically with increasing strain, from 45.58 to 23.01 GPa, 28.61 to 18.83 GPa, and 70.98 to 44.38 GPa, respectively. This consistent reduction indicates progressive elastic softening, reflecting the diminished resistance of the material to volumetric and shear deformation as the lattice expands. The Pugh ratio (B/G) and ν provide additional insight into its mechanical behavior. The B/G ratio decreases monotonically from 1.5930 to 1.2222, remaining below the critical value of 1.75 throughout the strain range investigated. According to Pugh's criterion, this indicates a predominantly brittle mechanical character, with the declining ratio suggesting an increasing tendency toward brittleness under isotropic tensile strain. Similarly, Poisson's ratio decreases monotonically from 0.2404 to 0.1786 and remains below the commonly cited threshold of 0.26, which is often used as an empirical indicator of bonding characteristics. This decrease reflects a progressive change in the

material's elastic response to lateral deformation. These results indicate that isotropic tensile strain progressively reduces the elastic stiffness of the material while favoring a more brittle mechanical response. The machinability index (μ_M = B/C_{44}) exhibits a monotonic decrease from 1.0615 in the unstrained structure to 1.0248 at 5% isotropic tensile strain, indicating a gradual reduction in the material's relative machinability as the tensile strain increases. Elastic anisotropy was assessed using the shear anisotropy factor, A, defined as $A = \frac{2C_{44}}{(C_{11}-C_{12})}$. The factor decreases from 2.7550 at 0% strain to 1.5516 at 5% strain, indicating a progressive reduction in shear anisotropy, although the material remains elastically anisotropic throughout the investigated strain range.

3.2. Dynamical Stability

In this section, the vibrational properties of the investigated compound are examined by calculating its phonon dispersion relations using the finite-displacement method implemented in the PHONOPY package [53]. Phonon spectra provide a comprehensive description of lattice dynamics and serve as a reliable criterion for assessing the dynamical behavior of crystalline materials. Generally, a crystal is considered dynamically stable when all phonon frequencies remain positive throughout the Brillouin zone, whereas the presence of imaginary phonon modes indicates dynamical instability associated with unstable lattice vibrations and possible structural transformations [68,69]. The phonon dispersion relations of ZnTe under tensile strains ranging from 0% to 5% are shown in Figure 3a–f.

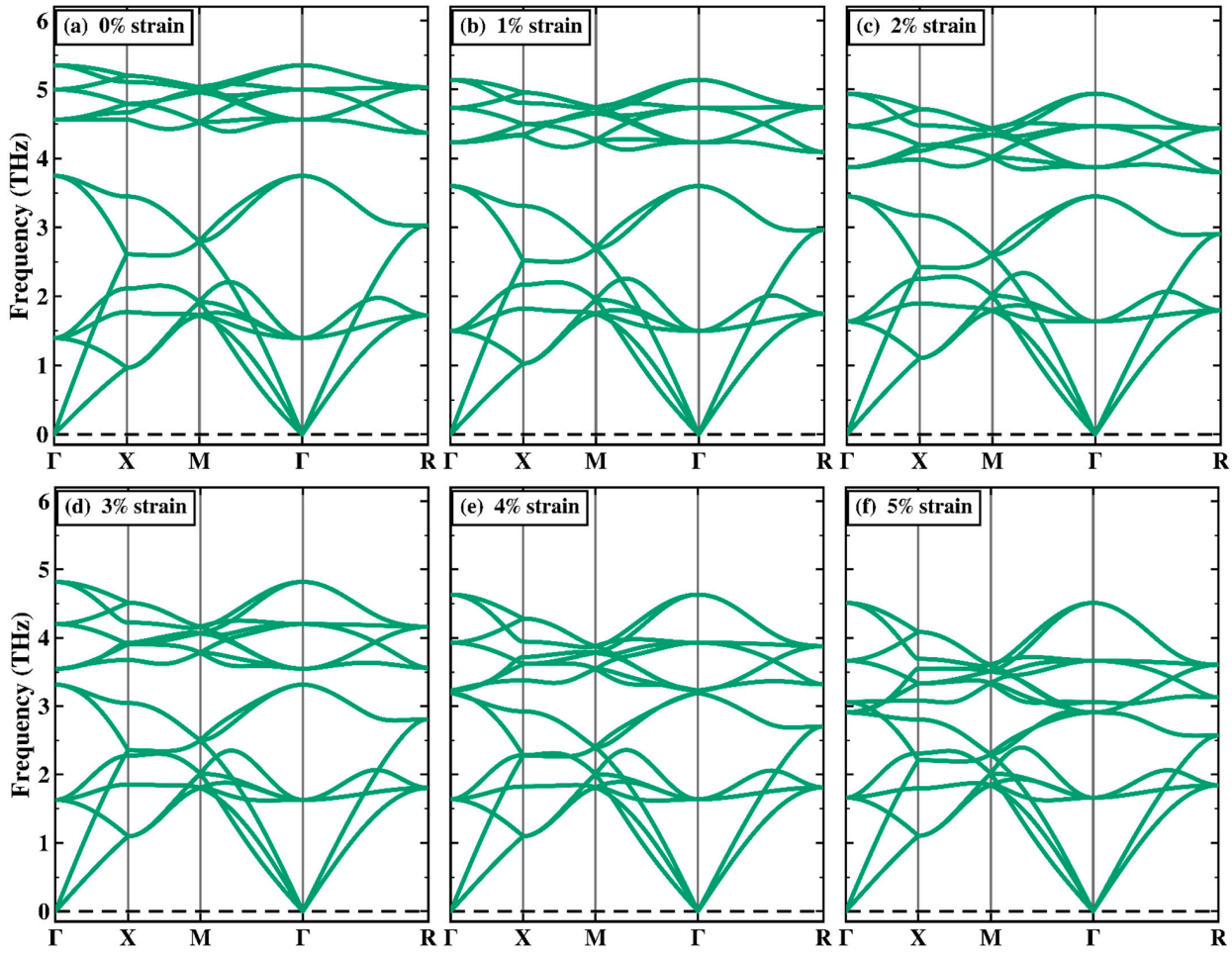


Figure 3. Phonon dispersion of ZnTe under tensile strain, ranging from 0% to 5%.

As seen in this figure, no imaginary phonon frequencies are found across the Brillouin zone for any of the applied tensile stresses, validating the cubic ZnTe structure's dynamical

stability. Additionally, the reported results are in excellent agreement previously published work [32,57–59]. The acoustic branches converge to zero frequency at the Γ point, consistent with the translational invariance of the crystal lattice. As isotropic tensile strain increases from 0% to 5%, the characteristic phonon frequency decreases monotonically from 5.350 THz in the unstrained structure to 5.139, 4.939, 4.818, 4.633, and 4.510 THz at 1%, 2%, 3%, 4%, and 5% strain, respectively. This systematic decrease reflects progressive phonon softening associated with lattice expansion and interatomic bond elongation, which modifies the interatomic force constants and reduces the restoring forces governing atomic vibrations. This behavior aligns with the strain-induced decrease in the elastic constants reported in Table 1, as both trends indicate a progressive reduction in lattice stiffness under tensile deformation. Despite this softening, the absence of imaginary phonon frequencies across the entire strain range investigated indicates that zinc-blende ZnTe remains dynamically stable under isotropic tensile strain up to 5%.

The stability of zinc-blende ZnTe in both the unstrained state and under isotropic tensile strain was assessed through a combined analysis of formation energies, elastic constants, and phonon dispersion spectra. The negative formation energies, the fulfillment of the Born mechanical stability criteria, and the absence of imaginary phonon frequencies provide complementary evidence supporting its thermodynamic, mechanical, and dynamical stability throughout the investigated strain range of 0–5%. These results indicate that the zinc-blende structure remains stable under the applied tensile deformation and provides a theoretical basis for further investigations into its experimental synthesis and potential technological applications.

3.3. Electronic Properties

To better understand how tensile strain affects ZnTe materials, we systematically investigated their electronic properties. Specifically, we analyzed the EBS and the DOS to clarify how strain induces changes in the electronic structure and the overall electronic behavior of these materials. The EBS of ZnTe materials were systematically investigated using DFT with the GGA-PBE and PBE + mBJ exchange potentials. While the GGA-PBE functional offers a reliable overview of the electronic structure, it is known to underestimate the band gap energy due to its approximate treatment of exchange-correlation interactions. To enhance the accuracy of the electronic structure calculations, the PBE + mBJ potential was utilized. This approach provides a more accurate description of the exchange potential, resulting in significantly more reliable band gap predictions that are generally in close agreement with available experimental data [31–34] and other theoretical calculations [32,70–72]. A summary of the calculated electronic band gap energies (Eg) obtained using both exchange-correlation functionals are presented in Table 2. As shown in the table, the band gaps calculated with GGA-PBE and PBE + mBJ show a consistent difference under isotropic tensile strain from 0% to 5%. The GGA-PBE functional systematically yields smaller band gaps than PBE + mBJ, consistent with the well-known tendency of conventional PBE-GGA functionals to underestimate semiconductor band gaps. For ZnTe, the band gap decreases monotonically from 1.049 eV at 0% strain to 0.440 eV at 5% strain using GGA-PBE, while the corresponding PBE-mBJ values decrease from 2.291 to 1.712 eV. Both approaches predict a monotonic reduction in the band gap with increasing tensile strain, indicating consistent trends despite quantitative differences in the calculated values. Accordingly, PBE + mBJ was selected for the subsequent electronic and optical analyses to provide a more reliable description of the band gap evolution under tensile strain.

Table 2. The band gap energy of ZnTe under tensile strain was calculated using the PBE-GGA and PBE + mBJ methods.

	Unstrained			Strain (%)				
	0%			1%	2%	3%	4%	5%
Exchange Functional	This Work	Experimental	Other Work					
PBE-GGA	1.051	2.24 [32]	1.07 [32]	0.918	0.791	0.670	0.554	0.440
PBE + mBJ	2.291	2.26 [33,34]	2.1 [70]	2.167	2.047	1.931	1.820	1.712

Figure 4a–f presents the PBE-mBJ EBS of the ZnTe materials under tensile strains ranging from 0% to 5%. A detailed analysis of the EBS along the high-symmetry paths of the first Brillouin zone reveals that the valence-band maximum (VBM) and conduction-band minimum (CBM) are both located at the Γ point, confirming the direct-band-gap semiconducting character of ZnTe throughout the investigated isotropic tensile-strain range. The direct band gap decreases monotonically from 2.291 eV in the unstrained structure to 1.712 eV under 5% tensile strain. The direct-gap character allows interband electronic transitions to occur without a change in crystal momentum, potentially facilitating electron excitation and charge-carrier generation. Furthermore, the strain-induced reduction in the band gap brings its value closer to the range generally considered favorable for single-junction solar cells within the Shockley–Queisser (SQ) framework, suggesting that tensile-strained ZnTe could be a promising candidate for photovoltaic applications. In addition, its strain-tunable electronic structure could be advantageous for photocatalytic applications. These findings suggest that isotropic tensile strain could provide a viable strategy for tailoring the electronic properties of ZnTe for potential photovoltaic and photocatalytic applications.

To further explore the electronic structure of the ZnTe materials, we calculated the TDOS and the PDOS using the PBE + mBJ functional. This DOS analysis provides valuable insights into the distribution of electronic states and their respective orbital contributions. The calculated TDOS and PDOS spectra under tensile strains ranging from 0% to 5% are presented in Figure 5a,b. In all cases, the vertical dashed line indicates the Fermi energy level (E_F), which is set to 0 eV. The TDOS results align with the electronic band structures and confirm that the investigated ZnTe compounds exhibit a direct bandgap SC character. Additionally, the PDOS spectra identify the specific orbital contributions to the VB and CB, highlighting how these contributions evolve under tensile strain. The PDOS spectra of ZnTe, as shown in Figure 5a, reveals a clear separation of orbital contributions within the VB when subjected to tensile strains ranging from 0% to 5%. A prominent peak is observed in the energy range of approximately −8 to −6 eV, which primarily arises from the Zn-3d orbitals. This indicates that this region is mainly influenced by Zn-3d states. In contrast, the upper VB, extending from −4 to 0 eV, is predominantly dominated by Te-5p orbitals, which make up the main contribution to the electronic states near the VBM. These findings demonstrate that the VB is primarily determined by the Zn-3d and Te-5p orbitals. In the CB states primarily arise from the hybridization of Zn-4s and Te-5p orbitals. The considerable overlap between these orbitals demonstrates strong hybridization, with Zn-3d orbitals contributing to a lesser extent through additional hybridization. These orbital interactions significantly influence the electronic structure of the CB.

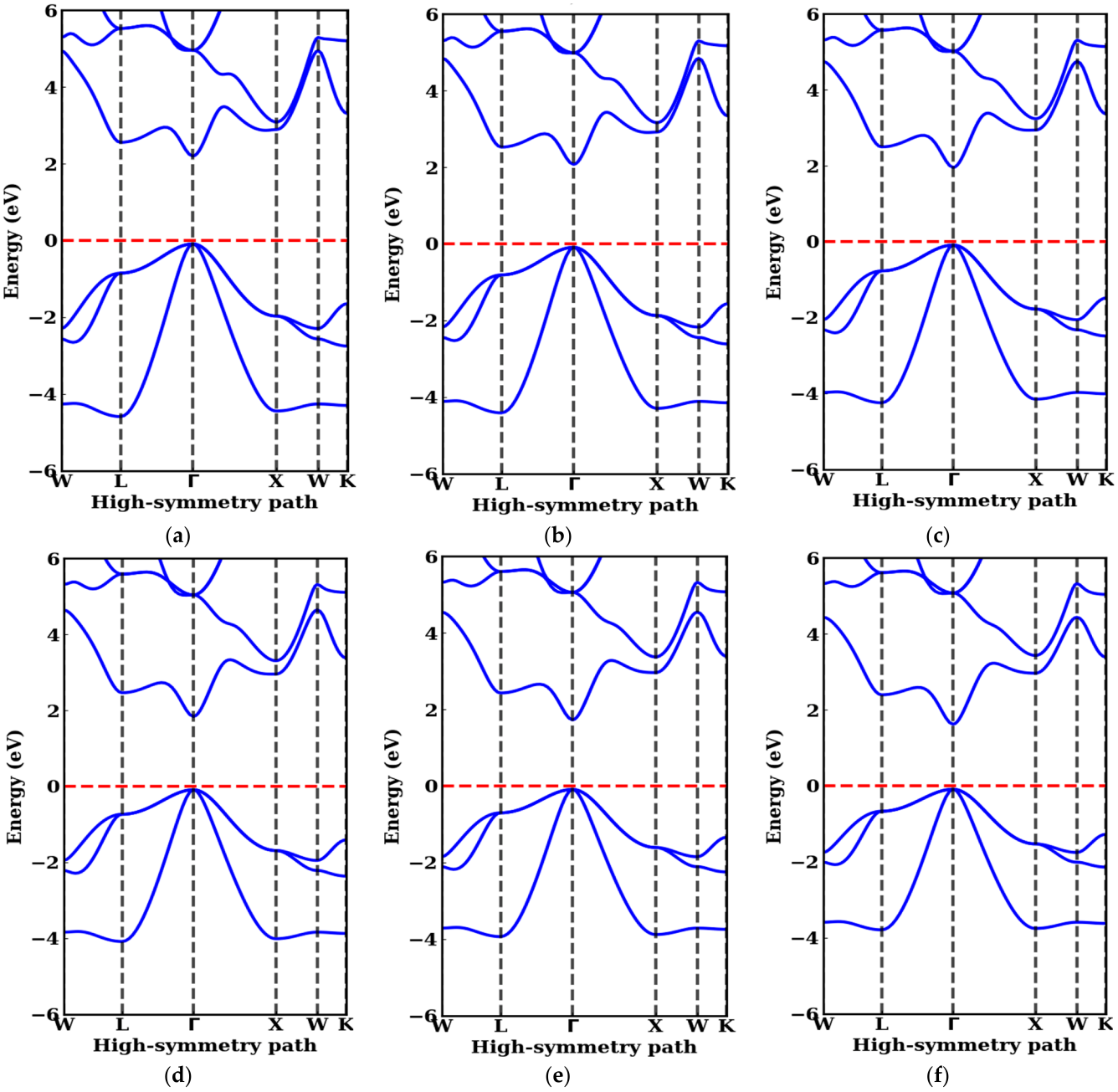


Figure 4. The EBS of ZnTe at various tensile strain levels were estimated using the mBJ exchange potential. (**a**) 0%; (**b**) 1%; (**c**) 2%; (**d**) 3%; (**e**) 4%; (**f**) 5%.

Figure 5b presents the TDOS of ZnTe under isotropic tensile strain. The vertical dashed line represents the Fermi energy level (E_F), which is close to the VBM. The results show a progressive narrowing of the direct band gap from 2.291 eV in the unstrained structure to 1.712 eV at 5% tensile strain, consistent with electronic band-structure calculations. This decrease in the band gap emphasizes the responsiveness of the electronic structure to tensile strain. It suggests the potential to extend optical absorption into longer wavelengths, which could have significant implications for the photovoltaic and photocatalytic properties of ZnTe.

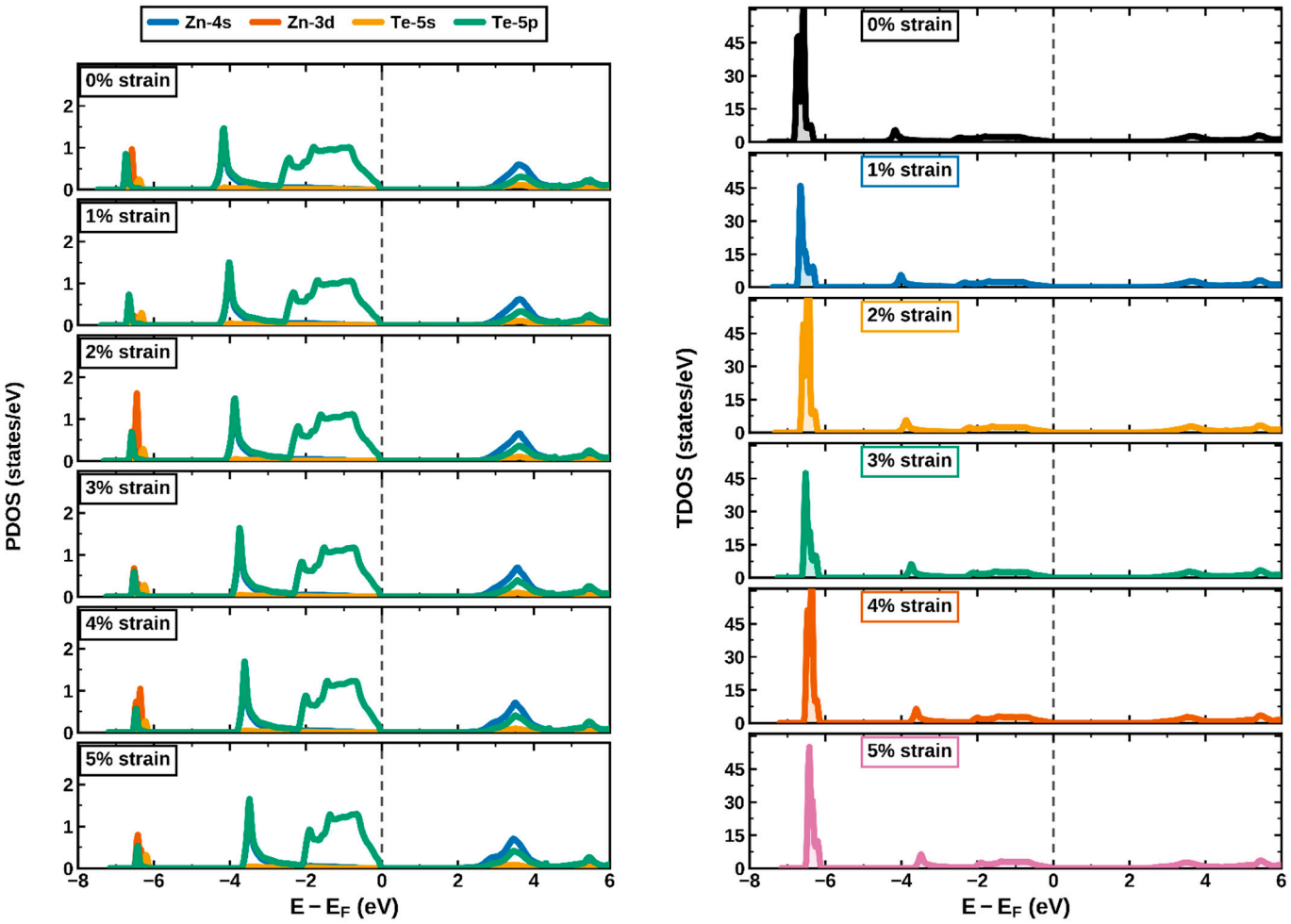


Figure 5. (**a**) Partial density of states (PDOS). (**b**) Total density of states (TDOS) of ZnTe under tensile strain ranging from 0% to 5%.

3.4. Optical Properties

While electronic structure offers insight into a material's intrinsic electronic characteristics, it alone is insufficient for evaluating its optoelectronic and energy-harvesting potential. A detailed investigation of optical properties is crucial, as SC performance is heavily influenced by electromagnetic interaction. We systematically investigated the strain-dependent optical properties of ZnTe materials using electronic structures derived from the mBJ exchange potential. The optical response was analyzed via the frequency-dependent complex dielectric function (DF), $\varepsilon(\omega)$, a fundamental quantity describing the interaction of incident photons with a material's electronic states. This function underpins the calculation of all other optical constants, such as refractive index, extinction coefficient, absorption coefficient ($\alpha(\omega)$), reflectivity, optical conductivity ($\sigma(\omega)$), and electron energy-loss function. The complex DF is described below [73]:

$$\varepsilon(\omega) = \varepsilon_1(\omega) + i\varepsilon_2(\omega) \tag{11}$$

where $\varepsilon_1(\omega)$ and $\varepsilon_2(\omega)$ represent the real and imaginary parts of the DF, respectively.

Figure 6a illustrates the $\varepsilon_1(\omega)$ for strained ZnTe. As tensile strain increases, the primary dielectric peaks shift toward lower photon energies, corresponding to the strain-induced reduction in the band gap. Notably, the ZnTe materials with 4% and 5% strain exhibit significant dielectric peaks in the visible region, corresponding to optical band gaps

of approximately 1.820 eV and 1.712 eV, respectively. This redshift extends the optical response into the visible spectrum, enhances light absorption, and improves the material's energy-harvesting capability.

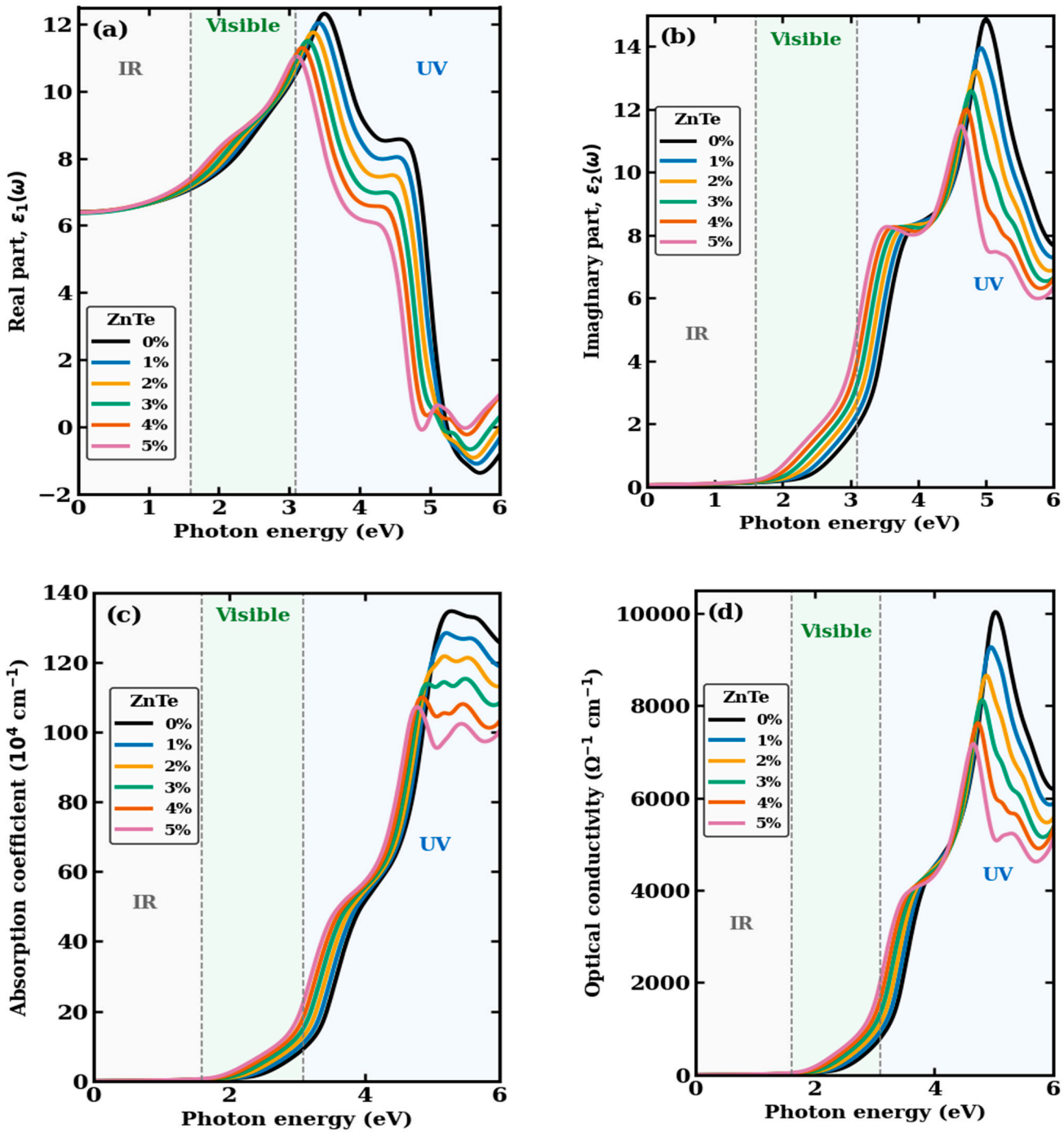


Figure 6. Optical properties of ZnTe at tensile strain: DF (real (**a**) and imaginary (**b**) components), (**c**) absorption coefficient, and (**d**) optical conductivity.

Figure 6b shows the $\varepsilon_2(\omega)$ of ZnTe in the photon energy range of 0–6 eV. The optical absorption threshold decreases from 2.30 eV for the pristine compound to 1.71 eV at 5% tensile strain, indicating a systematic redshift. This behavior is directly related to the progressive narrowing of the optical band gap, which agrees with the EBS and DOS analyses. The gradual increase in $\varepsilon_2(\omega)$ indicates more interband electronic transitions and stronger light-matter interactions. The lower threshold energy allows for the absorption of

low-energy photons, extending the optical response into the visible region. These strain-induced optical enhancements are especially useful for energy-harvesting applications because they improve solar spectrum utilization, photocarrier generation, and photon-to-energy conversion efficiency. As a result, light-harvesting performance is in the following order: 5% > 4% > 3% > 2% > 1% > 0%, indicating that 5% tensile strain provides the best optical response and has the greatest potential for energy-harvesting devices.

The optical $\alpha(\omega)$ was calculated using Equation (12) [74,75] to characterize the optical response of the material under investigation. This coefficient is one of the most important optical parameters, as it measures the ability of a SC to absorb incident photons across a wide range of photon energies [76,77]. In SC materials, optical absorption occurs due to electronic transitions between occupied VB states and unoccupied CB states, which happen when the energy of the incident photons exceeds the band-gap energy. Consequently, the $\alpha(\omega)$ is significantly influenced by the EBS and the dielectric response of the material, especially the imaginary part of the DF, $\varepsilon_2(\omega)$. Therefore, it is an effective parameter for assessing the optical performance and light-harvesting potential of SC materials [78,79].

$$\alpha(\omega) = \frac{\sqrt{2}\omega}{c}\sqrt{\sqrt{\varepsilon_1(\omega)^2 + \varepsilon_2(\omega)^2} - \varepsilon_1(\omega)} \quad (12)$$

Figure 6c illustrates the $\alpha(\omega)$ of ZnTe under tensile strains ranging from 0% to 5% over a photon energy range of 0 to 6 eV. The unstrained compound shows an absorption onset at approximately 2.3 eV, which aligns with the optical band gap determined from the EBS and DOS. As the tensile strain increases, the absorption onset progressively shifts to lower photon energies, indicating a gradual narrowing of the optical band gap (see Table 2). At the same time, $\alpha(\omega)$ increases across a broad photon energy range, and the absorption maxima exhibits a distinct redshift with heightened tensile strain. Enhanced optical absorption is seen in both the visible and UV regions, suggesting improved interaction between the incident photons and the material's electronic states. These optical characteristics stem from the strain-induced modifications in the electronic structure, which reduce the energy required for direct interband transitions from the VB to the CB. As a result, the enhanced absorption in the visible and UV spectra indicates that tensile strain significantly expands the spectrum sensitivity of ZnTe, making it a viable choice for broadband energy-harvesting applications.

Figure 6d depicts the $\sigma(\omega)$ spectra, of ZnTe under tensile strains ranging from 0% to 5% across the photon-energy range of 0–6 eV. The calculated $\sigma(\omega)$ spectra exhibits a strain-dependent evolution consistent with the corresponding absorption spectra. In pristine ZnTe, the onset of optical conductivity occurs at approximately the same photon energy as the absorption edge. As the isotropic tensile strain increases, the conductivity onset progressively shifts toward lower photon energies, indicating a redshift of the optical response. In addition, the optical conductivity increases in both the visible and ultraviolet regions, highlighting the influence of tensile strain on the frequency-dependent optical response of ZnTe. These results demonstrate that isotropic tensile strain provides an effective means of tailoring the optical properties of ZnTe, highlighting its potential as a candidate material for energy-harvesting applications.

In summary, the optical analysis demonstrates that tensile strain significantly improves the material's optical performance. The bandgap narrowing induced by tensile strain shifts the optical response toward the visible region. Additionally, the increased absorption coefficient and optical conductivity suggest enhanced light-harvesting capability. These improvements underline the potential of tensile-strained systems for applications in opto-electronics and solar energy harvesting. Nevertheless, achieving efficient photocatalytic water splitting requires not only favorable optical properties but also appropriate band-

edge alignment with the water redox potentials. Therefore, the photocatalytic performance of tensile-strained systems will be further evaluated in the next section.

3.5. Carrier Transport Properties

This section examines the carrier transport features of ZnTe under tensile strain by evaluating the effective masses of electrons and holes, as well as the exciton binding energy using the hydrogenic (Mott–Wannier) approximation [80]. These effective masses are crucial parameters that govern the optoelectronic behavior of SC materials. They directly influence carrier mobility, charge separation efficiency, and overall transport characteristics. According to Equation (13), carrier mobility is inversely proportional to effective mass. Therefore, materials with lower electron and hole effective masses are expected to demonstrate superior charge transport. These properties enable efficient separation and transport of photogenerated charge carriers, thereby minimizing electron–hole recombination and enhancing the performance of PC and PV systems [78]. We calculated the electron and hole effective masses in this study by fitting a second-order parabolic function to the electronic band dispersion near the CBM and VBM. Equation (14) was then used to calculate the effective masses. This method indicates that a steeper band curvature near the band edges corresponds to a smaller effective mass and higher carrier mobility. In contrast, flatter bands suggest heavier charge carriers with reduced transport properties [78].

$$\mu = \frac{e\,\tau}{m^*} \tag{13}$$

$$m^* = \hbar^2 \left(\frac{d^2E}{dk^2} \right)^{-1} \tag{14}$$

In Equations (13) and (14), m^* represents the effective mass of the charge carrier, $\hbar$ denotes the reduced Planck constant, μ indicates the carrier mobility, e stands for the elementary charge, and τ signifies the carrier relaxation time.

Table 3 presents the calculated electron and hole effective masses of ZnTe under tensile strain ranging from 0% to 5%. The electron effective mass decreases monotonically from 0.0550 to 0.0496, while the hole effective mass exhibits a slight overall decrease from 0.0428 to 0.0424, despite minor fluctuations at intermediate strain levels. These reductions in effective mass suggest enhanced carrier mobility, as lighter carriers generally respond more readily to an applied electric field. This trend may favor charge transport in strained ZnTe, which is beneficial for photovoltaic and photocatalytic applications.

Table 3. Computed electron and hole effective masses (m_e^* and m_h^*), effective mass ratio (D), and exciton binding energies (E_b) of ZnTe under different tensile strains up to 5%.

Strain	m_e^*/m_0	m_h^*/m_0	D	E_b (meV)
0%	0.0550	0.0428	0.7788	7.961612
1%	0.0537	0.0428	0.7963	7.904545
2%	0.0527	0.0428	0.8122	7.886127
3%	0.0517	0.0435	0.8409	7.908630
4%	0.0506	0.0425	0.8410	7.655104
5%	0.0496	0.0424	0.8536	7.604650

Additionally, the effective mass ratio ($D = m_h^*/m_e^*$), which is considered an indicator of charge-carrier separation [30], increases from 0.7788 in the unstrained system to 0.8536 under 5% tensile strain. This increase may promote more efficient separation of photogen-

erated electrons and holes and may reduce the probability of charge-carrier recombination. Consequently, photogenerated carriers may migrate efficiently to reaction sites, potentially enhancing the performance of photovoltaic, optoelectronic, and photocatalytic processes.

To elucidate the excitonic characteristics of ZnTe under tensile strain up to 5%, the exciton binding energy (E_b) was assessed utilizing the hydrogenic (Mott–Wannier) approximation, as outlined in Equation (15) [81]. E_b is a fundamental excitonic parameter that quantifies the Coulomb interaction between photogenerated electrons and holes, giving a direct indication of exciton stability. Generally, lower E_b values facilitate the dissociation of excitons into free charge carriers, which enhances charge separation and reduces carrier recombination [29]. Higher E_b values, on the other hand, correspond to more tightly bound excitons, indicating stronger electron-hole Coulomb interactions that can impede exciton dissociation and thus reduce charge separation efficiency.

$$E_b = 13.56 \times \frac{m_\mu}{m_0} \frac{1}{\varepsilon_1(0)^2} \quad (15)$$

The reduced exciton effective mass (m_μ) is calculated from the effective masses of m_e^* and the m_h^* using the equation $m_\mu = \frac{m_e^* \times m_h^*}{m_e^* + m_h^*}$, and ($\varepsilon_1(0)$) is the static dielectric constant is determined from optical calculations.

As reported in Table 3, the exciton binding energy (E_b) of ZnTe decreases slightly from 7.961612 meV in the unstrained system to 7.604650 meV under 5% tensile strain, indicating a modest reduction in the Coulomb interaction between electrons and holes. Both values are lower than the thermal energy at room temperature, suggesting that excitons may dissociate readily into free charge carriers under ambient conditions. This characteristic is favorable for the generation of mobile charge carriers and may support the potential of ZnTe for photovoltaic and photocatalytic applications.

3.6. Sustainable Photocatalytic Applications

3.6.1. Photocatalytic Water Splitting

The strain-induced enhancement of optical properties, along with the gradual narrowing of the band gap, suggests that ZnTe possesses the essential characteristics needed for visible-light-driven photocatalysis. However, having an appropriate band gap alone is not enough to ensure efficient overall water splitting; the positions of the band edges must also meet thermodynamic requirements by adequately straddling the redox potentials of water. Specifically, the CBM must be more negative than the hydrogen reduction potential ($E(H^+/H_2) = 0$ eV), while the VBM must be more positive than the water oxidation potential ($E(O_2/H_2O) = +1.23$ eV) [78]. This favorable band alignment provides sufficient thermodynamic driving forces for photogenerated electrons in the conduction band to reduce H^+ to H_2 and for holes in the valence band to oxidize H_2O to O_2 under light irradiation [82]. As a result, this enables the overall photocatalytic water-splitting reaction. Additionally, the corresponding reactions for water oxidation, proton reduction, and overall water splitting are described by Equations (16)–(18) [67,83].

$$H_2O + 2h^+ \rightarrow 2H^+ + \frac{1}{2}O_2 \quad (16)$$

$$2H^+ + 2e^- \rightarrow H_2 \quad (17)$$

$$H_2O \rightarrow H_2 + \frac{1}{2}O_2 \quad (18)$$

To assess if ZnTe meets the thermodynamic criteria for overall photocatalytic water splitting, its band-edge positions were calculated using the Mulliken electronegativity method, specifically determining the CBM and VBM via Equations (19) and (20) [84–88].

$$E_{CB} = \chi(S) - E_0 - \frac{E_g}{2} \quad (19)$$

$$E_{VB} = E_g + E_{CB} \quad (20)$$

$$\chi(S) = \left[(\chi_{Zn})^1 \times (\chi_{Te})^1\right]^{\frac{1}{2}} \quad (21)$$

Here, $\chi(S)$ represents the absolute Mulliken electronegativity of the ZnTe material, determined by the geometric mean of its constituent atoms' absolute electronegativities using Equation (21), with χ_{Zn} and χ_{Te} being the absolute electronegativities of Zn and Te, respectively [89]. E_0 is the free electron energy on the hydrogen scale (4.5 eV) [86,90], and Eg is the computed band gap. It should be noted that the Mulliken electronegativity method provides an approximate estimation of the band-edge positions. In the present calculations, the electronegativity is assumed to remain constant under tensile strain, although strain may modify the electron affinity and ionization potential. Therefore, the predicted band-edge positions should be interpreted as qualitative estimates rather than definitive values. A more rigorous assessment would require the independent evaluation of strain-dependent electron affinity and ionization potential.

The calculated band-edge positions of ZnTe under tensile strain are presented in Table 4 and illustrated in Figure 7a. In this figure, the dashed horizontal lines represent the water redox potential at pH = 0, which serve as thermodynamic reference levels for assessing the photocatalytic activity of ZnTe. As shown in Figure 7a and Table 4, the calculated positions of the band edges in ZnTe change systematically with increasing tensile strain. Specifically, the CBM gradually shifts towards less negative values, rising from −0.702 eV for the unstrained system to −0.41 eV at 5% tensile strain. Meanwhile, the VBM decreases from 1.59 eV to 1.3 eV over the same strain range. Despite these changes caused by strain, the CBM remains more negative than the H^+/H_2 reduction potential, while the VBM stays more positive than the O_2/H_2O oxidation potential at pH = 0 throughout the observed strain range. This indicates that the system meets the thermodynamic requirements for overall photocatalytic water splitting. As a result, the photogenerated electrons have enough reduced power to convert H^+ into H_2, and the photogenerated holes have sufficient oxidizing ability to convert H_2O into O_2. Additionally, the bandgap narrowing induced by tensile strain extends the optical absorption edge into the visible-light region. This enhancement improves solar light absorption and promotes the generation of photoexcited electron-hole pairs. The combination of suitable band-edge alignment and improved visible-light absorption is expected to enhance charge utilization during the photocatalytic process, leading to more efficient overall water splitting under visible light irradiation. These findings suggest that tensile-strained ZnTe has the essential electronic characteristics needed for efficient visible-light-driven photocatalytic water splitting, highlighting its potential as a promising material for sustainable hydrogen production. These results are consistent with previous theoretical studies on ZnTe at 0% strain [42].

Table 4. Estimated photocatalytic properties for ZnTe under tensile strain up to 5%.

Strain (%)	χ (eV)	Eg (eV)	E_{CB} (eV)	E_{VB} (eV)	$\chi(H_2)$ (eV)	$\chi(O_2)$ (eV)
0%	4.94272	2.291	−0.7027781	1.5882219	0.7027781	0.358222
1%	4.94272	2.167	−0.6407781	1.5262219	0.6407781	0.296222
2%	4.94272	2.047	−0.5807781	1.4662219	0.5807781	0.236222
3%	4.94272	1.931	−0.5227781	1.4082219	0.5227781	0.178222
4%	4.94272	1.82	−0.4672781	1.3527219	0.4672781	0.122722
5%	4.94272	1.712	−0.4132781	1.2987219	0.4132781	0.068722

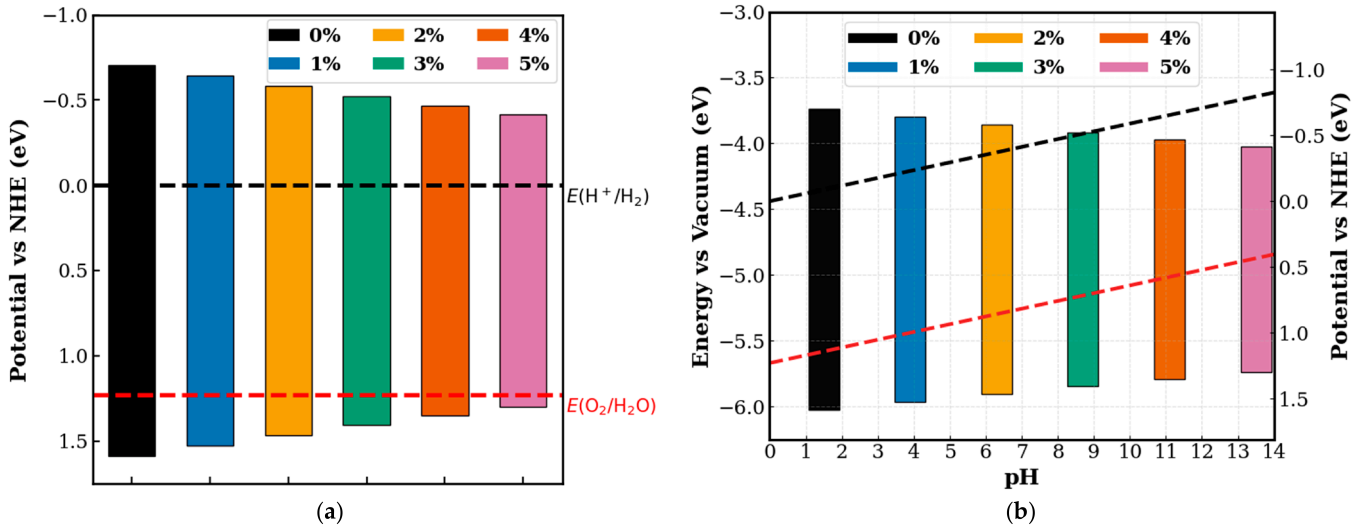


Figure 7. Calculated band-edge alignment of tensile-strained ZnTe (**a**) at pH = 0, and (**b**) under different pH levels.

To assess the photocatalytic efficacy of ZnTe under tensile strain (0–5%) for comprehensive water splitting, the overpotentials were derived from the computed band-edge positions. The overpotentials were determined as $\chi(H_2) = |E_{CB}) - (E(H^+/H_2)|$ for H_2 evolution and $\chi(O_2) = E_{VB} - E(O_2/H_2O)$ for O_2 evolution (relative to NHE at pH 0) [91]. Table 4 indicates that strain decreases the H_2 evolution overpotential from 0.703 eV at 0% strain to 0.413 eV at 5% strain, while the O_2 evolution reduces from 0.36 eV at 0% strain to 0.069 eV at 5% strain. Despite this decline, all strained ZnTe materials still exhibit positive overpotentials and proper band-edge alignment, ensuring a sufficient thermodynamic driving force for overall photocatalytic water splitting. Additionally, tensile strain shortens the band gap and boosts visible-light absorption, improving solar-light harvesting. In summary, the favorable alignment of band edges, sufficient overpotentials, and improved optical properties highlight the potential of strained ZnTe for efficient photocatalytic water splitting.

The pH of the reaction medium affects the thermodynamic redox potentials of the H^+/H_2 and O_2/H_2O couples. Consequently, the associated reduction and oxidation potentials relative to the NHE were calculated utilizing the Nernst equation, as presented in Equations (22) and (23), respectively [92].

$$E(H^+/H_2) = -0.059 \times pH \quad (22)$$

$$E(O_2/H_2O) = 1.23 - 0.059 \times pH \quad (23)$$

According to Equations (22) and (23), the redox potentials of H^+/H_2 and O_2/H_2O change linearly with pH, shifting by 0.059 eV for each unit increase in pH relative to their

values at pH = 0. All potential values are expressed in eV. To further investigate the effect of pH on the PC activity of strained ZnTe, the variation in band-edge alignment with pH was systematically examined, as shown in Figure 7b. The effect of tensile strain on the pH-dependent PC activity of ZnTe is characterized by a gradual reduction in its favorable operating pH window. In its unstrained configuration, ZnTe satisfies the necessary band-edge criteria for effective PC water splitting over a pH range of 1 to 12. However, as tensile strain increases, this advantageous pH range progressively narrows. At 1% strain, the range is reduced to pH 1 to 11; at 2% strain, it narrows further to pH 1 to 9; at 3% strain, it contracts to pH 1 to 8; and at 4% strain, it decreases to pH 1 to 7. At 5% strain, the conditions are limited to strongly acidic environments (pH < 5). This progressive narrowing occurs primarily due to the downward shift of the CBM, which reduces the thermodynamic driving force for proton reduction as pH increases. In contrast, the VBM consistently remains more positive than the O_2/H_2O oxidation potential across the entire pH range examined, indicating that the oxidation reaction remains thermodynamically feasible, regardless of the applied tensile strain. Therefore, the decline in PC activity at high pH levels is mainly due to the diminished reduction capability associated with the CBM, rather than any limitations in the oxidation process. Overall, these results indicate that unstrained and slightly tensile-strained ZnTe exhibits a wider pH range for thermodynamically feasible photocatalytic water splitting, whereas increasing tensile strain progressively narrows this range. These findings highlight the favorable band-edge alignment of ZnTe under unstrained and low-strain conditions for photocatalytic water splitting.

3.6.2. Solar-to-Hydrogen (STH) Conversion Efficiency

In this section, the STH conversion efficiency (η_{STH}) is considered an important descriptor for assessing the suitability of a photocatalyst for solar-driven water-splitting applications. It measures the fraction of incident solar energy converted into the chemical energy of hydrogen produced by the water-splitting reaction. Thus, η_{STH} provides a quantitative measure of the solar-energy conversion capability of the photocatalytic material. In the present study, the STH efficiency is determined using Equation (24), which is widely used to evaluate the potential of photocatalysts for solar-driven hydrogen production [30,93,94].

$$\eta_{\mathrm{STH}} = \eta_{\mathrm{abs}} \times \eta_{\mathrm{cu}} \tag{24}$$

Here, η_{abs} represents light absorption efficiency, and η_{cu} denotes the carrier utilization efficiency. The η_{abs} and η_{cu} are defined according to Equations (25) and (26), respectively.

$$\eta_{\mathrm{abs}} = \frac{\int_{E_g}^{\infty} P(E)dE}{\int_{0}^{\infty} P(E)dE} \tag{25}$$

$$\eta_{\mathrm{cu}} = \frac{\Delta G \frac{\int_{E_m}^{\infty} \frac{P(E)dE}{E}}{\int_{E_g}^{\infty} P(E)dE}}{} \tag{26}$$

where Eg denotes the band gap energy, P(E) is the AM1.5G solar power density at photon energy E = hν, and ΔG is the Gibbs free-energy change for overall water splitting, having a value of 1.23 eV in standard conditions. E_m is the minimum photon energy for the overall redox reactions, and is evaluated using Equation (27), incorporating overpotentials for the

hydrogen evolution reaction and the oxygen evolution reaction, denoted by $\chi(H_2)$ and $\chi(O_2)$, respectively.

$$E_m = \begin{cases} E_g & \text{if } \chi(H_2) \geq 0.2, \quad \chi(O_2) \geq 0.6 \\ E_g + 0.2 - \chi(H_2) & \text{if } \chi(H_2) < 0.2, \quad \chi(O_2) \geq 0.6 \\ E_g + 0.6 - \chi(O_2) & \text{if } \chi(H_2) \geq 0.2, \quad \chi(O_2) < 0.6 \\ E_g + 0.8 - \chi(O_2) - \chi(H_2) & \text{if } \chi(H_2) < 0.2, \quad \chi(O_2) < 0.6 \end{cases} \quad (27)$$

The calculated STH efficiencies are based on an idealized model that assumes absorption of photons with energies above the band gap, without explicitly accounting for absorber thickness, wavelength-dependent absorption, surface reflection, or other optical losses. The calculated values should therefore be interpreted as theoretical estimates rather than experimentally achievable efficiencies. The absorption and carrier-utilization terms must also be defined consistently to avoid double counting of physical losses.

Based on the results shown in Figure 8a–c and Table 5, tensile strain has a significant impact on the STH conversion characteristics of ZnTe. The light absorption efficiency (η_{abs}) increases progressively with tensile strain, rising from 24.82% in the unstrained structure to 50.52% at 5% strain. This indicates a substantial enhancement in the utilization of the incident solar spectrum. Conversely, the carrier utilization efficiency (η_{cu}) declines gradually from 28.58% to 23.92%, suggesting a moderate reduction in the fraction of photogenerated carriers that effectively contribute to the water-splitting reactions. However, the significant improvement in light absorption more than offsets the decrease in carrier utilization. As a result, the overall STH conversion efficiency (η_{STH}) increases continuously, from 7.09% at 0% strain to 12.08% at 5% strain. Therefore, tensile strain effectively enhances the solar energy conversion performance of ZnTe, with the 5% tensile-strained configuration demonstrating the highest η_{STH} among the materials investigated. In comparison to previously reported photocatalytic systems, the predicted STH efficiency of ZnTe increases from 7.09% in its unstrained state to 12.08% when subjected to a 5% tensile strain. This efficiency is comparable to those predicted for several recently studied photocatalysts. For instance, a theoretical STH efficiency of 11.64% was reported for monolayer CN_2 under 1% uniaxial tensile strain, while efficiencies of 13.60% and 12.08% were predicted for the A- and C-patterned Ga_2SSe/Bi_2O_3 van der Waals heterojunctions, respectively [95,96]. Experimental results indicate that an STH efficiency of 9.2% has been achieved for overall water splitting using an InGaN photocatalyst under concentrated solar irradiation [97].

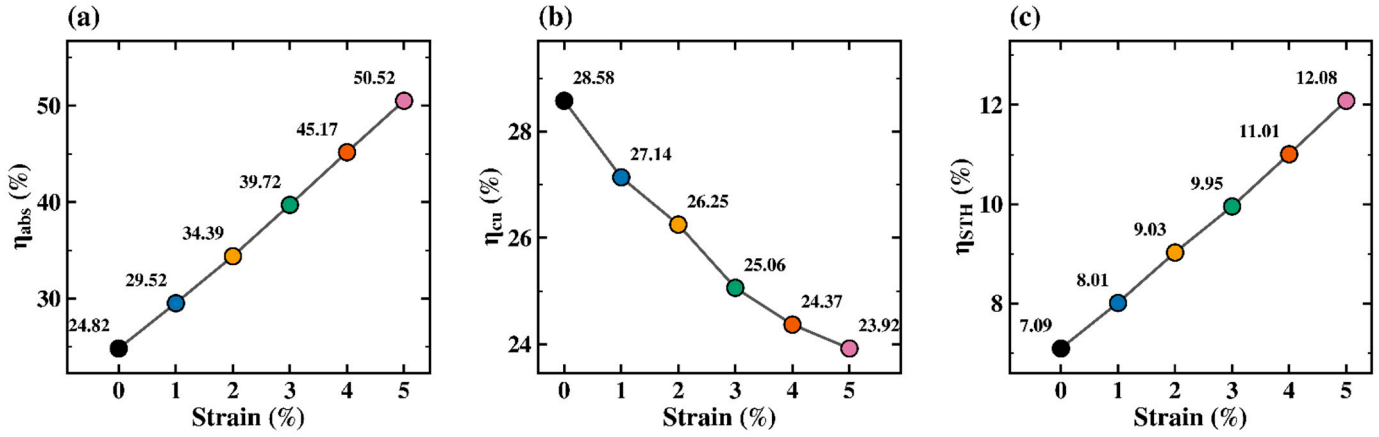


Figure 8. (**a**) Light absorption efficiency (ηabs), (**b**) charge carrier utilization efficiency (ηcu), and (**c**) theoretical solar-to-hydrogen (STH) efficiency under tensile strain ranging from 0% to 5%.

Table 5. STH efficiency of pure and tensile-strained ZnTe.

		0%	1%	2%	3%	4%	5%
ZnTe	η_{abs} (%)	24.82	29.52	34.39	39.72	45.17	50.52
	η_{cu} (%)	28.58	27.14	26.25	25.06	24.37	23.92
	η_{STH} (%)	7.09	8.01	9.03	9.95	11.01	12.08

3.6.3. Photocatalytic Degradation of Organic Pollutants

The contamination of aquatic environments by organic pollutants, including dyes, pharmaceuticals, phenolic compounds, pesticides, and industrial chemicals, has become a major environmental concern because of their persistence, potential toxicity, and adverse effects on aquatic ecosystems and human health [98,99]. Conventional wastewater treatment methods may be insufficient to completely remove certain recalcitrant contaminants, highlighting the need for efficient and sustainable remediation strategies. In this context, semiconductor-based photocatalysis has emerged as a promising advanced oxidation process (AOP) that uses solar energy to degrade organic pollutants [99]. As illustrated in Figure 9, the photocatalytic mechanism begins with the absorption of photons with energies equal to or greater than the semiconductor band gap, resulting in the excitation of electrons from the VB to the CB and the simultaneous generation of holes in the VB. These photogenerated charge carriers initiate complementary reduction and oxidation reactions. Specifically, conduction-band electrons can reduce dissolved oxygen (O_2) to form superoxide radicals ($\bullet O_2^-$), whereas valence-band holes can oxidize surface-adsorbed water molecules (H_2O) or hydroxide ions (OH^-) to generate hydroxyl radicals ($\bullet$OH), provided that the corresponding redox reactions are thermodynamically feasible. The resulting reactive oxygen species (ROS) attack organic pollutant molecules, promote the cleavage of chemical bonds, and facilitate the progressive degradation of intermediate products, potentially leading to the complete mineralization of organic contaminants into CO_2, H_2O, and inorganic ions [100,101]. The efficiency and thermodynamic feasibility of these processes depend on the positions of the semiconductor band edges relative to the relevant redox potentials. For effective superoxide radical generation, the CBM should be more negative than the $O_2/\bullet O_2^-$ redox potential (-0.33 eV vs. NHE). Hydroxyl radical formation through oxidation of H_2O or OH^- requires the VBM to be more positive than the corresponding $\bullet OH/H_2O$ (+2.38 eV) or $\bullet OH/OH^-$ (+1.55 V) redox potential, respectively. In addition, the $H_2O_2/\bullet$OH redox couple (+0.38 eV vs. NHE) may be relevant when hydrogen peroxide is present and participates in subsequent radical-generating reactions. These potentials are considered here at pH 7 [102,103], subject to the reference conditions and conventions adopted. Accordingly, appropriate band-edge alignment is a key criterion for evaluating the thermodynamic feasibility of ROS generation and the potential of semiconductor materials for photocatalytic degradation of organic pollutants under visible-light irradiation.

The calculated band-edge positions of ZnTe under isotropic tensile strain are presented in Figure 10. As the strain increases from 0% to 5%, the CBM shifts from -0.70 eV to -0.41 eV, while the VBM decreases from +1.59 eV to +1.30 eV, with all potential reference to the NHE. Throughout the investigated range of strain, the CBM remains more negative than the $O_2/\bullet O_2^-$ redox potential (-0.33 V). This indicates that photogenerated electrons retain sufficient thermodynamic driving force to reduce dissolved oxygen and form superoxide radicals ($\bullet O_2^-$), which can contribute to the oxidative degradation of organic pollutants. In contrast, the VBM is slightly more positive than the $\bullet OH/OH^-$ redox potential (+1.55 eV) at 0% strain. This suggests that the formation of $\bullet$OH through hydroxide oxidation is thermodynamically feasible at this strain level. However, as the isotropic tensile strain increases, the VBM shifts below this potential, making the hydroxide oxidation reaction

thermodynamically unfavorable. Furthermore, the VBM remains less positive than the •OH/H_2O redox potential (+2.38 eV) across all strain levels, indicating that direct hydroxyl radical formation through water oxidation is not thermodynamically viable under the conditions considered. These results suggest that superoxide radicals are the primarily accessible reactive species for photocatalytic degradation of organic pollutants by ZnTe throughout the investigated range of isotropic tensile strain. Although isotropic tensile strain modifies the band-edge positions of ZnTe, the CBM remains sufficiently negative to thermodynamically support the reduction of O_2 to $\bullet O_2^-$ throughout the investigated strain range (0–5%). In contrast, the VBM remains below the required potential for oxidizing OH^- to •OH at all investigated strain levels, indicating that •OH generation is thermodynamically unfavorable. Therefore, $\bullet O_2^-$ radicals are expected to be the predominant reactive oxygen species involved in the photocatalytic degradation of organic pollutants. These radicals can initiate the oxidation of organic molecules and promote chemical bond cleavage, leading to the formation of intermediate products. However, the absence of favorable •OH generation may limit the degradation and complete mineralization of certain recalcitrant pollutants. Further oxidation through alternative reaction pathways may contribute to the eventual conversion of intermediate products into CO_2, H_2O, and inorganic ions under suitable reaction conditions.

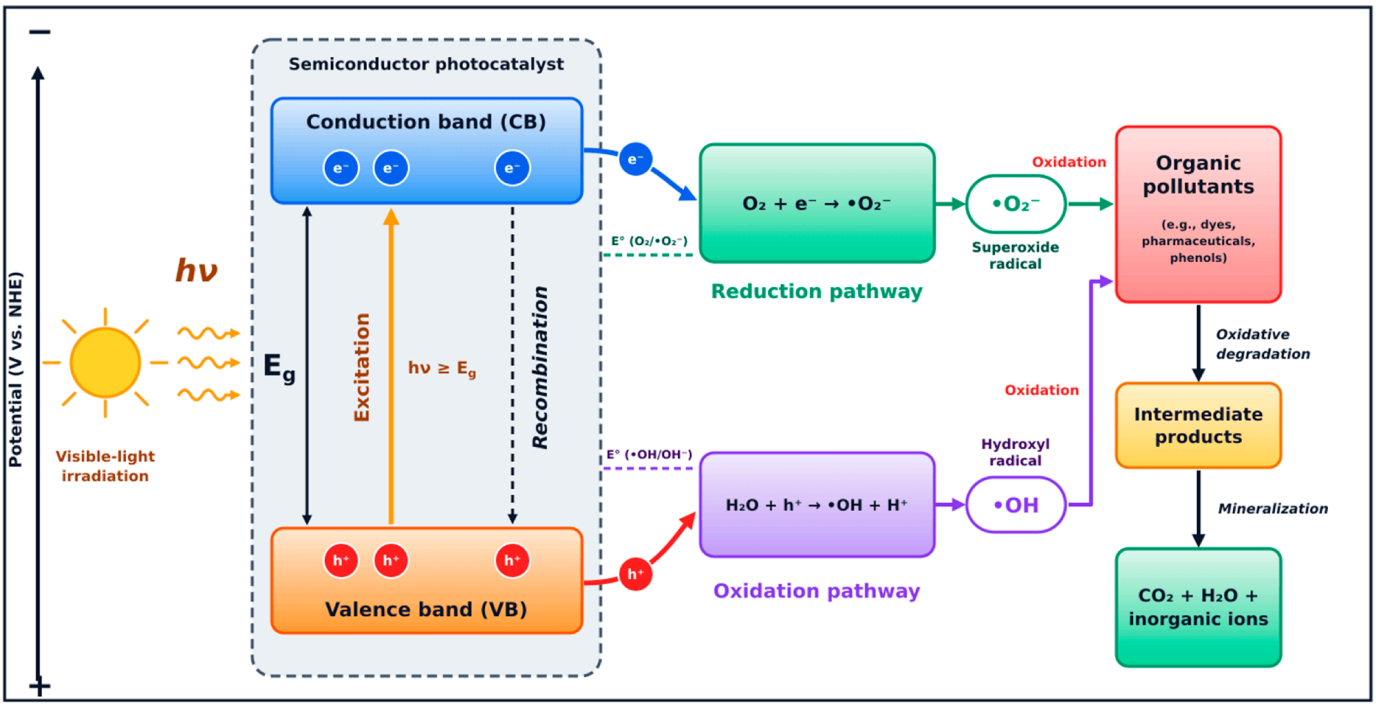


Figure 9. Schematic overview of the photocatalytic oxidation of organic contaminants under light irradiation.

It is important to note that these conclusions are based on band-edge alignment and do not, on their own, determine the actual efficiency of photocatalytic degradation or the primary reactive species present under experimental conditions. Therefore, experimental investigations are needed to validate the predicted band-edge positions, identify the dominant reactive species, and assess the photocatalytic degradation performance of ZnTe under relevant operating conditions.

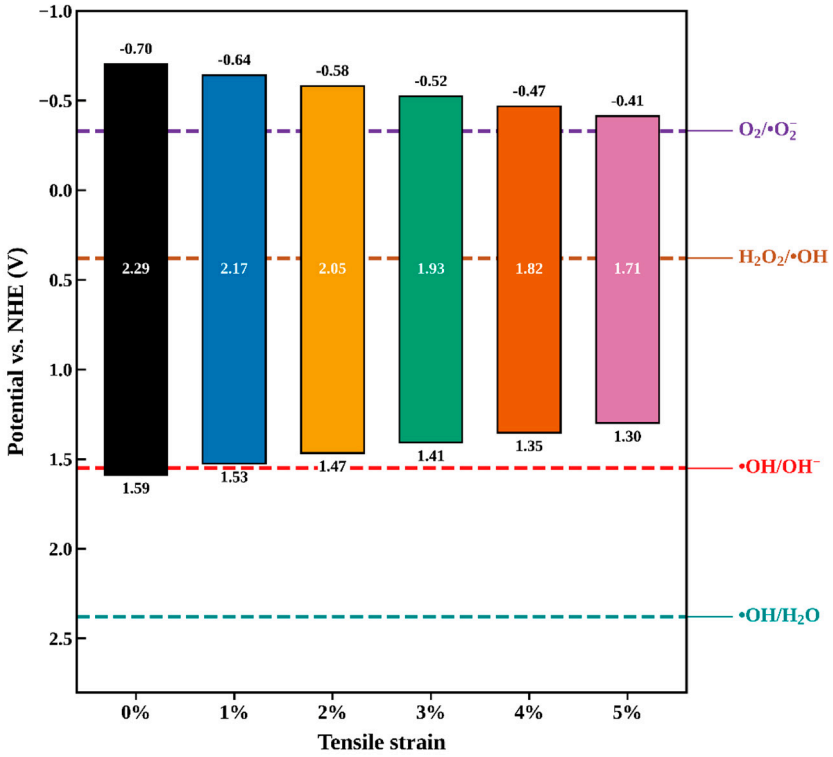


Figure 10. The evolution of ZnTe band-edge positions under tensile strain in relation to redox potential for the photocatalytic degradation of organic pollutants.

3.6.4. Photocatalytic CO_2 Reduction

Photocatalytic CO_2 reduction is a sustainable strategy for reducing CO_2 emissions and producing value-added chemicals and renewable fuels through solar energy. As one of the major greenhouse gases responsible for global climate change, CO_2 requires efficient conversion into valuable carbon-based products, which remains an important scientific and technological challenge. Under light irradiation, photogenerated electrons in the conduction band (CB) participate in a series of proton-coupled multi-electron transfer reactions, reducing CO_2 into a variety of products, including formic acid (HCOOH), carbon monoxide (CO), formaldehyde (HCHO), methanol (CH_3OH), methane (CH_4), ethylene (C_2H_4), ethanol (C_2H_5OH), ethane (C_2H_6), and propanol (C_3H_7OH), as described by the corresponding half-reactions in Equations (28)–(36) [65,104–108]. Meanwhile, the photogenerated holes in the VB oxidize water, supplying the protons required for the reduction reactions while maintaining charge balance. For efficient photocatalytic CO_2 reduction, the CBM must be more negative than the reduction potentials of the corresponding CO_2 redox couples to provide sufficient thermodynamic driving force for electron transfer, whereas the VBM should remain more positive than the H_2O/O_2 oxidation potential to sustain water oxidation [109]. Therefore, the calculated band-edge positions of ZnTe are employed to evaluate its thermodynamic feasibility for the photocatalytic conversion of CO_2 into these value-added products.

$$CO_2 + 2H^+ + 2e^- \rightarrow HCOOH \quad (28)$$

$$CO_2 + 2H^+ + 2e^- \rightarrow CO + H_2O \quad (29)$$

$$CO_2 + 4H^+ + 4e^- \rightarrow HCHO + H_2O \quad (30)$$

$$CO_2 + 6H^+ + 6e^- \rightarrow CH_3OH + H_2O \quad (31)$$

$$CO_2 + 8H^+ + 8e^- \rightarrow CH_4 + 2H_2O \quad (32)$$

$$2CO_2 + 12H^+ + 12e^- \rightarrow C_2H_4 + 4H_2O \quad (33)$$

$$2CO_2 + 12H^+ + 12e^- \rightarrow C_2H_5OH + 3H_2O \quad (34)$$

$$2CO_2 + 14H^+ + 14e^- \rightarrow C_2H_6 + 4H_2O \quad (35)$$

$$3CO_2 + 18H^+ + 18e^- \rightarrow C_3H_7OH + 5H_2O \quad (36)$$

Figure 11a,b illustrate the alignment of the CBM and VBM with the CO_2 reduction redox potentials at pH 0 and pH 7 for ZnTe under various tensile strains. The horizontal dashed lines show the standard reduction potentials for various CO_2 reduction half-reactions. This alignment helps determine the thermodynamic feasibility of CO_2 reduction and predict possible reaction products based on applied tensile strain. As illustrated in Figure 11a, applying a tensile strain of up to 5% gradually shifts the CBM downward while maintaining a favorable energetic alignment with the redox potentials for CO_2 reduction. Throughout the entire range of strain, the CBM remains more negative than the reduction potentials associated with various CO_2 conversion pathways, including CO_2 to HCOOH, CO_2 to CO, CO_2 to CH_3OH, CO_2 to CH_4, CO_2 to C_2H_6, CO_2 to C_3H_7OH, CO_2 to C_2H_4, CO_2 to HCHO, and CO_2 to C_2H_5OH. This confirms that these reduction reactions are thermodynamically feasible. The favorable alignment of the band edges provides sufficient thermodynamic driving force for photogenerated electrons to initiate the corresponding CO_2 reduction reactions. This demonstrates that the applied tensile strain preserves the photocatalytic reduction capability of the ZnTe materials under solar irradiation. Increasing the pH from 0 to 7 shifts the redox potentials of the considered CO_2 reduction pathways toward more negative values, thereby modifying their alignment with the band edges, as illustrated in Figure 11b. The calculated band-edge positions indicate that ZnTe maintains favorable energetic alignment for all considered CO_2 reduction pathways across the investigated tensile strain range (0–5%) at pH 0. At pH 7, the thermodynamic feasibility varies depending on the specific reduction pathway and the applied strain. These findings demonstrate that tensile strain modulates the thermodynamic driving force of ZnTe for photocatalytic CO_2 reduction under both acidic and near-neutral conditions, highlighting its potential for strain-tunable photocatalytic applications.

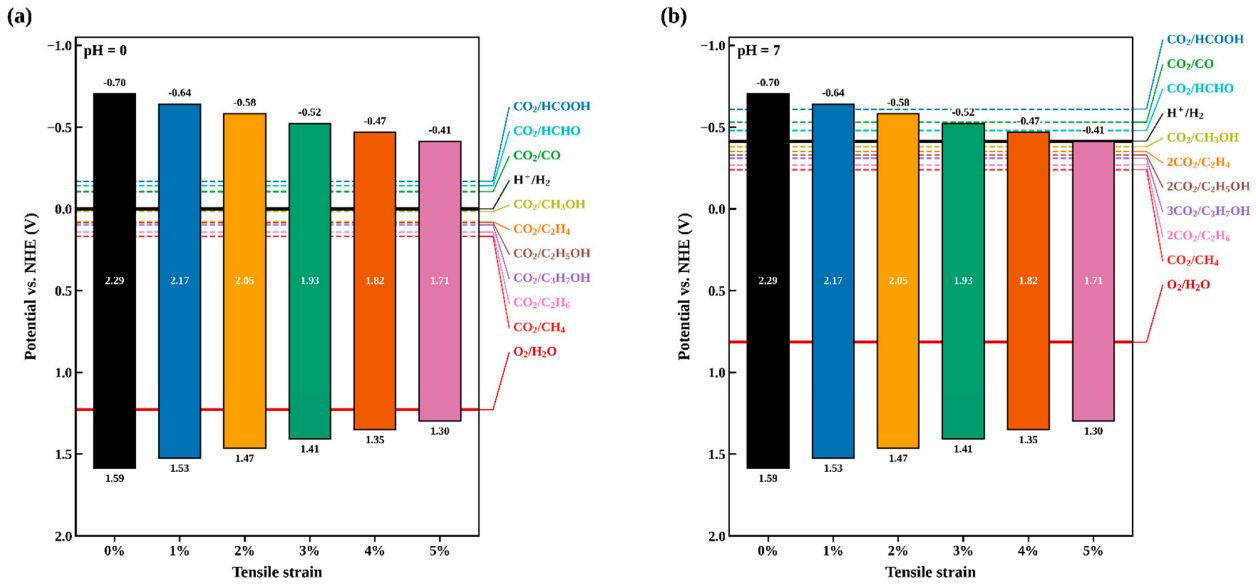


Figure 11. The CO_2 photoreduction capability of tensile-strained ZnTe based on calculated band-edge alignment: (**a**) at pH = 0 and (**b**) at pH = 7.

To assess the thermodynamic feasibility of CO_2 reduction for ZnTe under isotropic tensile strain, we calculated the potential differences related to the formation of various carbon-containing products. This evaluation was based on the CBM potential and the relevant redox potential. Table 6 presents these potential differences for isotropic tensile strains ranging from 0% to 5% at pH levels of 0 and 7, respectively. The potential difference is defined as $\Delta E = E_{redox} - E_{CBM}$, where E_{redox} represents the equilibrium potential for the specific CO_2 reduction reaction, and E_{CBM} denotes the CBM potential. Both values are expressed on the same reference scale. According to this definition, a positive ΔE indicates a favorable thermodynamic alignment for the corresponding CO_2 reduction pathway, while a negative value suggests an unfavorable alignment.

Table 6. Thermodynamic potential differences for CO_2 reduction on ZnTe under isotropic tensile strain at pH 0 and 7.

	pH = 0						pH = 7					
	0%	**1%**	**2%**	**3%**	**4%**	**5%**	**0%**	**1%**	**2%**	**3%**	**4%**	**5%**
CO_2/HCOOH	0.534	0.472	0.412	0.3538	0.2983	0.2443	0.0928	0.0308	−0.0292	−0.0872	−0.1427	−0.1967
CO_2/HCHO	0.562	0.500	0.440	0.3818	0.3263	0.2723	0.2228	0.1608	0.1008	0.0428	−0.0127	−0.0667
CO_2/CO	0.598	0.536	0.476	0.4178	0.3623	0.3083	0.1728	0.1108	0.0508	−0.0072	−0.0627	−0.1167
CO_2/CH_3OH	0.720	0.658	0.598	0.5398	0.4843	0.4303	0.3228	0.2608	0.2008	0.1428	0.0873	0.0333
CO_2/C2H_4	0.782	0.720	0.660	0.6018	0.5463	0.4923	0.3528	0.2908	0.2308	0.1728	0.1173	0.0633
CO_2/C_2H_5OH	0.787	0.725	0.665	0.6068	0.5513	0.4973	0.3728	0.3108	0.2508	0.1928	0.1373	0.0833
CO_2/C_3H_7OH	0.802	0.740	0.680	0.6218	0.5663	0.5123	0.3928	0.3308	0.2708	0.2128	0.1573	0.1033
CO_2/C_2H_6	0.845	0.783	0.723	0.6648	0.6093	0.5553	0.4328	0.3708	0.3108	0.2528	0.1973	0.1433
CO_2/CH_4	872	0.810	0.750	0.636	0.6363	0.5823	0.4628	0.4008	0.3408	0.2828	0.2273	0.1733

As shown in Table 6, at pH 0, the calculated ΔE decrease monotonically with isotropic tensile strain from 0% to 5% across all investigated CO_2 reduction pathways. Specifically, ΔE decreases from 0.5338 to 0.2443 eV for HCOOH, from 0.5618 to 0.2723 eV for HCHO, and from 0.5978 to 0.3083 eV for CO. The same trend is observed for CH_3OH (0.7198–0.4303 eV), C_2H_4 (0.7818–0.4923 eV), C_2H_5OH (0.7868–0.4973 eV), C_3H_7OH (0.8018–0.5123 eV), C_2H_6 (0.8448–0.5553 eV), and CH_4 (0.8718–0.5823 eV). Notably, all pathways exhibit an identical decrease of 0.2895 eV over the investigated strain range, reflecting a systematic shift in the relative alignment between the CBM and the corresponding CO_2 reduction potentials. Despite this reduction, ΔE remains positive for all pathways at every strain level considered. According to the adopted thermodynamic criterion, these results indicate favorable energetic alignment for CO_2 reduction toward the investigated products at pH 0, with isotropic tensile strain progressively modifying the thermodynamic driving force.

Additionally, as the pH increases from 0 to 7, the calculated potential differences change in magnitude while showing a consistently decreasing trend with increasing isotropic tensile strain. At pH 7, for the conversion of CO_2 to HCOOH, the ΔE decreases from 0.0928 eV at 0% strain to 0.0308 eV at 1% strain. It becomes negative at 2% strain (−0.0292 eV) and reaches −0.1967 V at 5% strain. For the conversion of CO_2 to CO, ΔE decreases from 0.1728 eV at 0% strain to 0.0508 eV at 2% strain, becoming negative between 2% and 3% strain, and reaching −0.1167 eV at 5% strain. Similarly, for the conversion of CO_2 to HCHO, ΔE decreases from 0.2228 eV at 0% strain to 0.0428 V at 3% strain, turns negative at 4% strain (−0.0127 eV), and reaches −0.0667 eV at 5% strain. These results indicate that the favorable thermodynamic potential alignment for the formation of HCOOH, CO, and HCHO is no longer maintained beyond the corresponding crossover strains. In contrast, ΔE remains positive throughout the investigated strain range for the conversion of CO_2 to CH_3OH, C_2H_4, C_2H_5OH, C_3H_7OH, C_2H_6, and CH_4, even though it decreases

monotonically with increasing strain. From 0% to 5% strain, the values of ΔE decrease as follows: CH_3OH from 0.3228 eV to 0.0333 eV; C_2H_4 from 0.3528 V to 0.0633 V; C_2H_5OH from 0.3728 V to 0.0833 V; C_3H_7OH from 0.3928 eV to 0.1033 eV; C_2H_6 from 0.4328 eV to 0.1433 eV; and CH_4 from 0.4628 eV to 0.1733 eV. Notably, the ΔE for CH_3OH formation approaches zero at 5% strain but remains positive throughout the entire investigated range. These results highlight the combined influence of pH and isotropic tensile strain on the thermodynamic feasibility of CO_2 reduction using ZnTe.

3.7. Spectroscopic Limited Maximum Efficiency (SLME)

The photovoltaic (PV) performance of the materials studied is theoretically assessed using the spectroscopic limited maximum efficiency (SLME) model developed by Yu and Zunger [110]. Evaluating photovoltaic efficiency is crucial for identifying promising materials for solar cells. While the traditional Shockley–Queisser (SQ) model predicts the theoretical efficiency limit of a single-junction solar cell mainly based on its band-gap energy [111,112], the SLME model offers a more detailed analysis by including material-specific optical absorption spectra, absorber thickness, and losses from radiative and non-radiative recombination. In this study, the SLME is calculated using electronic and optical properties derived from first-principles calculations with the standard AM1.5G solar spectrum, representing an incident solar irradiance of 1000 W/m^2. This method allows for a systematic evaluation of the materials' photovoltaic potential by considering their electronic structures and optical absorption features. The power conversion efficiency (PCE), labeled as η, measures the ratio of the maximum electrical power output to the incident solar power and is defined as follows:

$$\eta = \frac{P_m}{P_{in}} \tag{37}$$

where P_{in} represents the incident solar irradiance, and P_m represents the maximum power density that can be extracted from the solar cell based on its current density-voltage (J-V) characteristics. These quantities are used to quantify the theoretical PCE of the investigated materials within the SLME model, as given by the following expression:

$$P_m = \max(JV) = \max\left(\left[J_{sc} - J_0\left(\exp\left(\frac{eV}{K_B T} - 1\right)\right)\right]V\right) \tag{38}$$

Here, J denotes the current density, V represents the voltage across the absorber layer, K_B is the Boltzmann constant, T refers to the absolute temperature, and e is the elementary charge. The short-circuit current density (Jsc) and the reverse saturation current density (J_0) are calculated using the following equations:

$$J_{sc} = \int_0^\infty eA(E)I_{sun}dE \tag{39}$$

$$J_0 = \frac{J_0^r}{f_r} = \frac{e\pi}{f_r}\int_0^\infty A(E)I_{bb}(E,T)dE \tag{40}$$

Here, I_{sun} refers to the incident photon flux density derived from the standard AM1.5G solar spectrum, while $I_{bb}(E, T)$ represents the photon flux density from a black body. J_0^r denotes the radiative recombination current density, and A(E) signifies the energy-dependent absorptivity of the absorber material. The factor f_r accounts for the impact of the band-gap nature on radiative recombination and is defined as $f_r = e^{\frac{-\Delta}{K_B T}}$, where $\Delta = E_g^{da} - E_g$. In this equation, E_g^{da} is the energy of the lowest direct-allowed transition, Eg is the minimum band-gap energy, k_B represents the Boltzmann constant, and T is the absolute temperature. Since all the investigated materials exhibit direct band gaps, $E_g^{da} = E_g$, yielding $\Delta = 0$ and

consequently $f_r = 1$. This means that there is no need for a correction related to indirect band gap transitions in the SLME calculations for the materials studied.

The open-circuit voltage (Voc) and fill factor (FF) are determined using the following expressions [6]:

$$V_{oc} = \frac{K_B T}{q} \ln\left(\frac{J_{sc}}{J_0} + 1\right) \quad (41)$$

$$FF = \frac{P_m}{J_{sc} \times V_{oc}} \quad (42)$$

The PV performance of ZnTe under isotropic tensile strain was investigated using the SLME model. Figure 12a,b illustrate the variations in the short-circuit current density (Jsc) and SLME, respectively, as functions of absorber thickness over the range of 10^{-3}–10^{3} µm for different tensile strain levels, while the corresponding Voc and FF are summarized in Table 7. As the isotropic tensile strain increases from 0% to 5%, Jsc increases monotonically from 9.11 to 22.16 mA/cm^2. This enhancement is associated with strain-induced band gap narrowing, which shifts the absorption edge toward lower photon energies and potentially broadens the range of solar photons available for absorption. Accordingly, the SLME increases monotonically from 16.71% to 28.83%, corresponding to a relative improvement of approximately 72.5%. In contrast, Voc decreases monotonically from 1.971 to 1.429 V, whereas FF exhibits a comparatively modest monotonic decline from 93.1% to 91.1%. Despite these reductions, the substantial increase in Jsc leads to an overall improvement in the predicted photovoltaic efficiency. Furthermore, the thickness-dependent SLME results highlight the role of absorber thickness in photovoltaic performance and suggest that optimizing the absorber thickness alongside tensile strain could further enhance the efficiency of ZnTe.

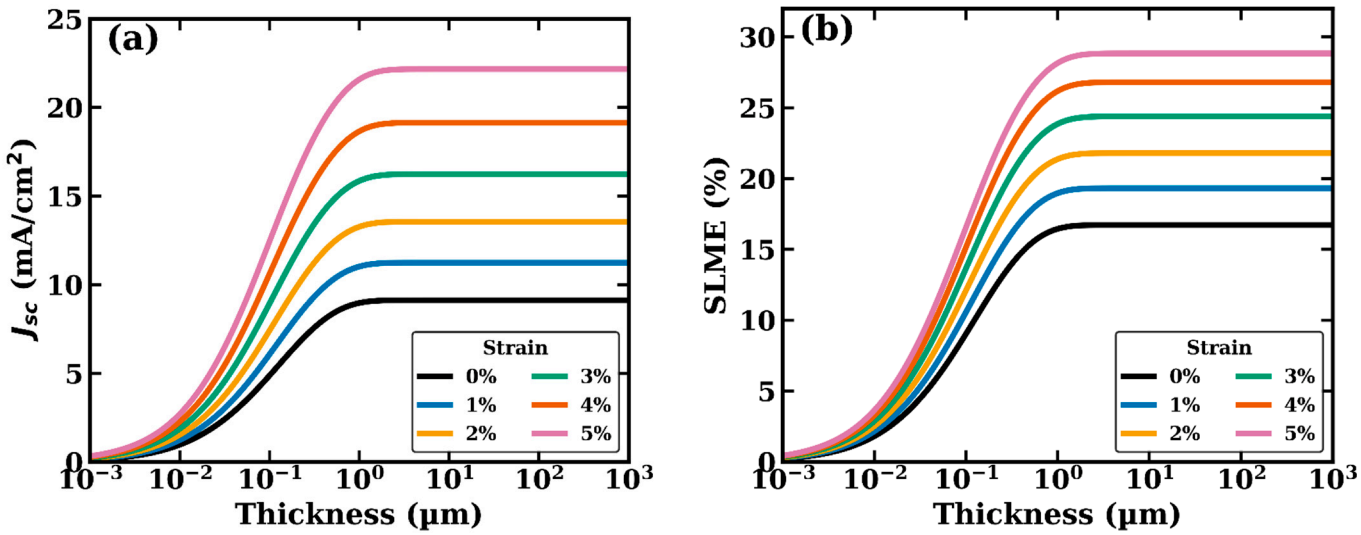


Figure 12. (**a**) Short-circuit current density (JSC) as a function of absorber thickness under different tensile strain levels (0–5%). (**b**) Spectroscopic limited maximum efficiency (SLME) as a function of absorber thickness under the same strain conditions.

The observed trends align qualitatively with those reported for $Na_2Cu_2TeO_6$, where applying strain increases the Jsc while decreasing the Voc and the FF [113]. Despite these changes, ZnTe achieves a maximum SLME of 28.83% under 5% tensile strain, surpassing the previously reported value of 26.16% for $Na_2Cu_2TeO_6$. Additionally, the consistent rise in SLME with increasing tensile strain demonstrates the effectiveness of strain engineering in enhancing the photovoltaic performance of ZnTe. These findings suggest that combining isotropic tensile strain with optimal absorber thickness can improve the photovoltaic

efficiency of ZnTe, emphasizing its potential as a promising absorber material for high-performance solar cells.

Table 7. Photovoltaic parameters of ZnTe under isotropic tensile strain.

Strain %	Jsc (mA/cm^2)	Voc (V)	FF (%)	η (%)
0%	9.11	1.971	93.1	16.711
1%	11.23	1.855	92.7	19.310
2%	13.54	1.743	92.4	21.97
3%	16.23	1.634	92	24.378
4%	19.13	1.531	91.5	26.794
5%	22.16	1.429	91.1	28.831

4. Conclusions

In summary, this paper provides a thorough first-principles examination of the influence of tensile strain on the multifunctional characteristics of zinc blende ZnTe. The computed formation energies, elastic constants, and phonon dispersion spectra confirm its thermodynamic, mechanical, and dynamical stability throughout the entire investigated tensile strain range of 0 to 5%. The compound keeps its direct band-gap character, but the bandgap gradually narrows from 2.291 to 1.712 eV, resulting in increased visible-light absorption. Additionally, tensile strain significantly improves the absorption and optical conductivity, while decreasing exciton binding energy and facilitating charge-carrier transport. The photovoltaic performance of ZnTe was assessed using the SLME model, resulting in a maximum predicted SLME of 28.83% under a tensile strain of 5%. Additionally, photocatalytic analysis shows that the CBM shifts from -0.70 eV to -0.41 eV, while the VBM decreases from 1.59 eV to 1.3 eV as tensile strain increases. Despite these changes, the band-edge positions still fulfill the thermodynamic requirements for water splitting and CO_2 reduction pathways. For pollutant degradation, $\bullet O_2^-$ remains the predominant reactive oxygen species under tensile strain, as its generation is thermodynamically favorable at all strain levels, whereas the unfavorable formation of •OH may limit the complete mineralization of organic pollutants. This study highlights the potential of strain-engineered ZnTe for photovoltaic applications and solar-driven photocatalytic processes, such as hydrogen production, CO_2 reduction, and organic pollutant degradation.

Author Contributions: Conceptualization, A.B. and Y.J.; methodology, A.B.; software, A.B., M.M. and Y.J.; validation, A.B. and H.B.; formal analysis, A.B. and Y.J.; investigation, A.B.; data curation, A.B.; writing—original draft preparation, A.B.; writing—review and editing, H.B.; visualization, H.B.; supervision, Y.Z. All authors have read and agreed to the published version of the manuscript.

Funding: The authors are warmly grateful to the support of "The Moroccan Association of Sciences and Techniques for Sustainable Development (MASTSD), Beni Mellal, Morocco". No specific grant number was assigned to this funding.

Institutional Review Board Statement: Not applicable.

Informed Consent Statement: Not applicable.

Data Availability Statement: Data is available on request.

Conflicts of Interest: The authors declare no conflicts of interest.

References

1. Ye, T.; Wang, K.; Hou, Y.; Yang, D.; Smith, N.; Magill, B.; Yoon, J.; Mudiyanselage, R.R.H.H.; Khodaparast, G.A.; Wang, K.; et al. Ambient-air-stable lead-free $CsSnI_3$ solar cells with greater than 7.5% efficiency. *J. Am. Chem. Soc.* **2021**, *143*, 4319–4328. [CrossRef] [PubMed]
2. Chu, S.; Cui, Y.; Liu, N. The path towards sustainable energy. *Nat. Mater.* **2017**, *16*, 16–22. [CrossRef] [PubMed]
3. Chu, S.; Majumdar, A. Opportunities and challenges for a sustainable energy future. *Nature* **2012**, *488*, 294–303. [CrossRef] [PubMed]
4. Armaroli, N.; Balzani, V. The future of energy supply: Challenges and opportunities. *Angew. Chem. Int. Ed.* **2007**, *46*, 52–66. [CrossRef] [PubMed]
5. Wu, Z.; Liu, Y.; Zou, C.; Guo, W. Thermally activated delayed fluorescence materials for CO_2 reduction. *Next Energy* **2023**, *1*, 100041. [CrossRef]
6. Fatihi, H.; Agouri, M.; Ouhenou, H.; Benaali, H.; Zaghrane, A.; Abbassi, A.; El Idrissi, M.; Taj, S.; Manaut, B. Enhancing Solar Cell Efficiency: A Comparative Study of Lead-Free Double Halide Perovskites $Rb_2CuAsBr_6$ and $Rb_2TlAsBr_6$ using DFT and SLME Methods. *J. Inorg. Organomet. Polym.* **2025**, *35*, 964–977. [CrossRef]
7. Kannan, N.; Vakeesan, D. Solar energy for future world: A review. *Renew. Sustain. Energy Rev.* **2016**, *62*, 1092–1105. [CrossRef]
8. Tsoutsos, T.; Frantzeskaki, N.; Gekas, V. Environmental impacts from the solar energy technologies. *Energy Policy* **2005**, *33*, 289–296. [CrossRef]
9. Izam, N.S.M.N.; Itam, Z.; Sing, W.L.; Syamsir, A. Sustainable Development Perspectives of Solar Energy Technologies with Focus on Solar Photovoltaic—A Review. *Energies* **2022**, *15*, 2790. [CrossRef]
10. Zhao, X.; Zhang, X.; Lei, M.; Ma, X.; Li, Y.; Jin, Z. Synergistic effect of morphology regulation of $LaNiO_3$ S-scheme heterojunction for enhanced photocatalytic hydrogen production. *J. Mater. Sci. Technol.* **2026**, *245*, 238–248. [CrossRef]
11. Harb, M. Designing the Optimal Cr-Doped TiO_2 Photocatalyst for Solar-Driven Hydrogen Production: A Comprehensive DFT Study. *ACS Appl. Electron. Mater.* **2026**, *8*, 834–843. [CrossRef]
12. Laazizi, I.; Jaber, B.; Fazouan, N.; Laanab, L. Lead-Free $RbSnCl_3$-Based Halide Perovskites for Solar-to-Hydrogen Conversion: Insights from DFT Calculations. *J. Phys. Chem. Solids* **2026**, *212*, 113531. [CrossRef]
13. Vn, D.; Ramachandran, N.; Chattopadhyaya, M. Computational Insights Into g-C_3N_4-Based Heterojunctions for Photocatalytic Water Splitting Reaction. *J. Comput. Chem.* **2026**, *47*, e70437. [CrossRef] [PubMed]
14. Sohail, M.; Rauf, S.; Irfan, M.; Hayat, A.; Alghamdi, M.M.; El-Zahhar, A.A.; Ghernaout, D.; Al-Hadeethi, Y.; Lv, W. Recent developments, advances and strategies in heterogeneous photocatalysts for water splitting. *Nanoscale Adv.* **2024**, *6*, 1286–1330. [CrossRef] [PubMed]
15. Shen, H.; Ouyang, T.; Guo, J.; Mu, M.; Yin, X. A perspective LDHs/$Ti_3C_2O_2$ design by DFT calculation for photocatalytic reduction of CO_2 to C2 organics. *Appl. Surf. Sci.* **2023**, *609*, 155445. [CrossRef]
16. Chang, X.; Wang, T.; Gong, J. CO_2 photo-reduction: Insights into CO_2 activation and reaction on surfaces of photocatalysts. *Energy Environ. Sci.* **2016**, *9*, 2177–2196. [CrossRef]
17. Wu, J.; Wang, G.; Ding, Q.; Chi, W.; Zeng, C.; Sun, P.P. Atomic-level insights from DFT calculations guide the design of metal ion-doped 2D GA (MA) 3Pb3I10 perovskites for enhanced photocatalytic CO_2 reduction. *Appl. Surf. Sci.* **2026**, *727*, 166047. [CrossRef]
18. Zhou, X.; Sun, F.; Zhao, M.; Li, J.; Wang, S.; Yuan, Z.; Dong, X.; Zhu, Y. Heterojunction and piezoelectric polarization effect co-driven Janus nanofibers photocatalyst for degradation of organic pollutants and H_2O_2 production. *Ceram. Int.* **2026**, *52*, 39994–40008. [CrossRef]
19. Khan, M.S.; Li, Y.; Li, D.S.; Qiu, J.; Xu, X.; Yang, H.Y. A review of metal–organic framework (MOF) materials as an effective photocatalyst for degradation of organic pollutants. *Nanoscale Adv.* **2023**, *5*, 6318–6348. [CrossRef] [PubMed]
20. Kitchamsetti, N.; Ramteke, M.S.; Rondiya, S.R.; Mulani, S.R.; Patil, M.S.; Cross, R.W.; Dzade, N.Y.; Devan, R.S. DFT and experimental investigations on the photocatalytic activities of NiO nanobelts for removal of organic pollutants. *J. Alloys Compd.* **2021**, *855*, 157337. [CrossRef]
21. Fujishima, A.; Honda, K. Electrochemical Photolysis of Water at a Semiconductor Electrode. *Nature* **1972**, *238*, 37–38. [CrossRef] [PubMed]
22. Karuppasamy, A. Enhanced photocatalysis and photohydrophilicity in TiO_2–W_5O_{14} nanocomposite thin films grown by in-lay sputtering. *Mater. Chem. Phys.* **2023**, *301*, 127580. [CrossRef]
23. Zhang, Q.; Wang, Y.; Jia, Y.; Yan, W.; Li, Q.; Zhou, J.; Wu, K. Engineering the Electronic Structure towards Visible Lights Photocatalysis of $CaTiO_3$ Perovskites by Cation (La/Ce)-Anion (N/S) Co-Doping: A First-Principles Study. *Molecules* **2023**, *28*, 7134. [CrossRef] [PubMed]
24. Aktary, M.; Kamruzzaman, M.; Afrose, R.J.M.A. Pressure-dependent comparative study of the mechanical, electronic, and optical properties of $CsPbX_3$ (X = Cl, Br, I): A DFT study for optoelectronic applications. *Mater. Adv.* **2023**, *4*, 4494–4508. [CrossRef]

25. Aktary, M.; Kamruzzaman, M.; Afrose, R. A comparative study of the mechanical stability, electronic, optical and photocatalytic properties of $CsPbX_3$ (X = Cl, Br, I) by DFT calculations for optoelectronic applications. *RSC Adv.* **2022**, *12*, 23704–23717. [CrossRef] [PubMed]
26. Liu, X.; Hu, A.; Liu, Z.; Ding, K.; Xia, W.; Shangguan, H.; Zhang, C.; Fu, T. Review on fundamental and recent advances of strain engineering for enhancing photocatalytic CO_2 reduction. *Adv. Energy Mater.* **2025**, *15*, 2405320. [CrossRef]
27. Miao, Y.; Zhao, Y.; Zhang, S.; Shi, R.; Zhang, T. Strain engineering: A boosting strategy for photocatalysis. *Adv. Mater.* **2022**, *34*, 2200868. [CrossRef] [PubMed]
28. Liu, Z.; Menéndez, C.; Shenoy, J.; Hart, J.N.; Sorrell, C.C.; Cazorla, C. Strain engineering of oxide thin films for photocatalytic applications. *Nano Energy* **2020**, *72*, 104732. [CrossRef]
29. Chelh, A.; Akenoun, B.; Dahbi, S.; Ez-Zahraouy, H. Compressive strain effects on the photocatalytic and optoelectronic properties of CsInBr3 for efficient hydrogen production: A DFT study. *Surf. Interfaces* **2025**, *72*, 107356. [CrossRef]
30. Achqraoui, M.; El Akkel, M.; Jamaï, I.; Bekkioui, N.; Ez-Zahraouy, H. Strain-driven optimization of bulk WSe2 for photovoltaic, photocatalytic, and thermoelectric applications: First-Principles insights. *Int. J. Hydrogen Energy* **2026**, *222*, 154265. [CrossRef]
31. Yu, E.T.; Phillips, M.C.; McCaldin, J.O.; McGill, T.C. Measurement of the CdSe/ZnTe valence band offset by x-ray photoelectron spectroscopy. *J. Vac. Sci. Technol. B Microelectron. Nanometer Struct. Process. Meas. Phenom.* **1991**, *9*, 2233–2237. [CrossRef]
32. Shobana, M.; Meher, S.R. Experimental and ab-initio study of the structural, electronic and vibrational properties of ZnTe. *J. Alloys Compd.* **2018**, *762*, 260–271. [CrossRef]
33. Isik, M.; Gullu, H.H.; Parlak, M.; Gasanly, N.M. Synthesis and temperature-tuned band gap characteristics of magnetron sputtered ZnTe thin films. *Phys. B Condens. Matter* **2020**, *582*, 411968. [CrossRef]
34. Mahalingam, T.; Dhanasekaran, V.; Sundaram, K.; Kathalingam, A.; Rhee, J.K. Characterization of electroplated ZnTe coatings. *Ionics* **2012**, *18*, 299–306. [CrossRef]
35. Tanaka, T.; Nishio, M.; Guo, Q.; Ogawa, H. Fabrication of ZnTe light-emitting diode by Al thermal diffusion through surface oxidation layer. *Jpn. J. Appl. Phys.* **2008**, *47*, 8408. [CrossRef]
36. Lee, K.S.; Oh, G.; Chu, D.; Pak, S.W.; Kim, E.K. High power conversion efficiency of intermediate band photovoltaic solar cell based on Cr-doped ZnTe. *Sol. Energy Mater. Sol. Cells* **2017**, *170*, 27–32. [CrossRef]
37. Tanaka, T.; Yu, K.M.; Stone, P.R.; Beeman, J.W.; Dubon, O.D.; Reichertz, L.A.; Kao, V.M.; Nishio, M.; Walukiewicz, W. Demonstration of homojunction ZnTe solar cells. *J. Appl. Phys.* **2010**, *108*, 024502. [CrossRef]
38. Rakhshani, A.E.; Thomas, S. Nitrogen doping of ZnTe for the preparation of ZnTe/ZnO light-emitting diode. *J. Mater. Sci.* **2013**, *48*, 6386–6392. [CrossRef]
39. Fang, Z.; Weng, S.; Ye, X.; Feng, W.; Zheng, Z.; Lu, M.; Lin, S.; Fu, X.; Liu, P. Defect engineering and phase junction architecture of wide-bandgap ZnS for conflicting visible light activity in photocatalytic H2 evolution. *ACS Appl. Mater. Interfaces* **2015**, *7*, 13915–13924. [CrossRef] [PubMed]
40. Cao, F.; Shi, W.; Zhao, L.; Song, S.; Yang, J.; Lei, Y.; Zhang, H. Hydrothermal synthesis and high photocatalytic activity of 3D wurtzite ZnSe hierarchical nanostructures. *J. Phys. Chem. C* **2008**, *112*, 17095–17101. [CrossRef]
41. Wang, J.; Meng, J.; Li, Q.; Yang, J. Single-layer cadmium chalcogenides: Promising visible-light driven photocatalysts for water splitting. *Phys. Chem. Chem. Phys.* **2016**, *18*, 17029–17036. [CrossRef] [PubMed]
42. Xia, F.; Shu, L.; Wen, Y.; Yang, F.; Zhen, C. Enhancing the catalytic activity of CdX and ZnX (X = S, Se and Te) nanostructures for the hydrogen evolution reaction via transition metal doping. *Mater. Adv.* **2022**, *3*, 5772–5777. [CrossRef]
43. Venkatesh, R.; Upadhyay, V.V.; Bhooshanam, N.N.; Mohanavel, V.; Karthik, K.; Ayyar, M.; Ravichandran, M.; Soudagar, M.E.M.; Seikh, A.H. Enhancing CdTe solar cell performance via znte/cu back contact optimization. *Appl. Phys. A* **2025**, *131*, 712. [CrossRef]
44. Suchikova, Y.; Kovachov, S.; Bohdanov, I.; Popova, E.; Moskina, A.; Popov, A. Characterization of CdxTeyOz/CdS/ZnO Heterostructures Synthesized by the SILAR Method. *Coatings* **2023**, *13*, 639. [CrossRef]
45. Lamonova, K.; Prokhorov, A.; Schmidbauer, M.; Kwasniewski, A.; Kazarinov, Y.; Konuhova, M.; Platonenko, A.; Remeš, Z.; Ridzoňová, K.; Buryi, M. Luminescence properties of ZnSe single crystals co-doped with Fe and Cr. *Opt. Mater. X* **2025**, *25*, 100393. [CrossRef]
46. Gueddim, A.; Bouarissa, N.; Ziani, H. Electronic structure and optical properties of monolayer ZnTe under compressive and tensile strains. *Phys. B Condens. Matter* **2025**, *700*, 416896. [CrossRef]
47. Blaha, P.; Schwarz, K.; Madsen, G.K.; Kvasnicka, D.; Luitz, J. *Wien2k. An Augmented Plane Wave+ Local Orbitals Program for Calculating Crystal Properties*; Vienna University of Technology: Vienna, Austria, 2001; Volume 60, pp. 155–169.
48. Perdew, J.P.; Burke, K.; Ernzerhof, M. Generalized gradient approximation made simple. *Phys. Rev. Lett.* **1996**, *77*, 3865. [CrossRef] [PubMed]
49. Koller, D.; Tran, F.; Blaha, P. Improving the modified Becke-Johnson exchange potential. *Phys. Rev. B—Condensed Matter Mater. Phys.* **2012**, *85*, 155109. [CrossRef]
50. Belhachi, S. Accurate Bandgap of Zr x Al1−x N Using Modified Becke–Johnson (mBJ) Exchange Potential. *J. Supercond. Nov. Magn.* **2018**, *31*, 1545–1548. [CrossRef]

51. Koller, D.; Tran, F.; Blaha, P. Merits and limits of the modified Becke-Johnson exchange potential. *Phys. Rev. B—Condensed Matter Mater. Phys.* **2011**, *83*, 195134. [CrossRef]
52. Jamal, M.; Bilal, M.; Ahmad, I.; Jalali-Asadabadi, S. IRelast package. *J. Alloys Compd.* **2018**, *735*, 569–579. [CrossRef]
53. Togo, A.; Tanaka, I. First principles phonon calculations in materials science. *Scr. Mater.* **2015**, *108*, 1–5. [CrossRef]
54. Momma, K.; Izumi, F. VESTA 3 for three-dimensional visualization of crystal, volumetric and morphology data. *Appl. Crystallogr.* **2011**, *44*, 1272–1276. [CrossRef]
55. Agouri, M.; Fatihi, H.; Ouhenou, H.; Khossossi, N.; Abbassi, A.; Taj, S.; Manaut, B. Theoretical investigation of high-efficiency halide perovskite $Rb_2NaTlBr_6$ for photovoltaic solar cells. *Sol. Energy* **2025**, *300*, 113788. [CrossRef]
56. Murnaghan, F.D. The compressibility of media under extreme pressures. *Proc. Natl. Acad. Sci. USA* **1944**, *30*, 244–247. [CrossRef]
57. Tanisa, N.Y.; Rahman, M.; Musa, A.M.; Bhuiyan, J.H.; Aziz, T. Comprehensive DFT study of structural, mechanical, dynamical, electronic, and optical properties of ZnX (X = S, Se, Te) semiconductors. *Adv. Mater. Sci. Eng.* **2026**, *2026*, 2466402. [CrossRef]
58. Sarkar, B.K.; Verma, A.S.; Sharma, S.; Kundu, S.K. First-principles calculations of the structural, phonon and thermal properties of ZnX (X = S, Se, Te) chalcogenides. *Phys. Scr.* **2014**, *89*, 075704. [CrossRef]
59. Muthaiah, R.; Annam, R.S.; Tarannum, F.; Gupta, A.K.; Garg, J.; Arafin, S. Length dependence thermal conductivity of zinc selenide (ZnSe) and zinc telluride (ZnTe)–a combined first principles and frequency domain thermoreflectance (FDTR), study. *Phys. Chem. Chem. Phys.* **2022**, *24*, 28814–28824. [CrossRef] [PubMed]
60. Born, M.; Huang, K. *Dynamical Theory of Crystal Lattices*; Oxford University Press: Oxford, UK, 1996. [CrossRef]
61. Gusev, A.I.; Sadovnikov, S.I. Conditions of elastic mechanical stability and elastic properties of crystal structures with different symmetry. *Fiz. Tverd. Tela* **2022**, *64*, 671–675. [CrossRef]
62. Riaz, K.; Drissi, N.; Abdalla, S.; Belhachi, S.; Bousbih, R.; Soliman, M.S.; Nasarullah; Hasanin, T.H.A.; Nazar, M.; Abdulhussein, N.A. Computational exploration of structural, elastic, optoelectronic and magnetic properties of A_2YHgCl_6 (A = Cs, K) using, enhanced computational techniques. *J. Inorg. Organomet. Polym. Mater.* **2025**, *35*, 5363–5376. [CrossRef]
63. Jouad, Y.; Ziat, Y.; Bouzaid, A.; Belkhanchi, H. First-principles examination of hydrostatic pressure effects on the structural, mechanical, phonon, and optoelectronic properties of $TlGeX_3$ (X = Br, I). *Next Mater.* **2026**, *12*, 102052. [CrossRef]
64. Hill, R. The elastic behaviour of a crystalline aggregate. *Proc. Phys. Soc. Sect. A* **1952**, *65*, 349. [CrossRef]
65. El Akkel, M.; Ez-Zahraouy, H. Multifunctional double perovskites Cs_2BI_6 (B = Ti, Ge, Se, Sn, and Te) for solar energy harvesting: Photovoltaic, photocatalytic, and thermoelectric pathways. *Energy* **2025**, *335*, 137928. [CrossRef]
66. Siah, H.; Sabri, M.; Chelh, A.; Ez-Zahraouy, H. Strain-engineered optoelectronic and photocatalytic properties of vacancy-free double perovskite Cs2KInI6 for hydrogen production: A first-principles study. *Inorg. Chem. Commun.* **2026**, *192*, 117299. [CrossRef]
67. Saeed, U.; Gohar, O.; Alburaih, H.A.; Nazir, S. High-performance photocatalytic water splitting for hydrogen production, amplified solar cell efficiency, and energy harvesting in X@ Na-doped Na_2ZrTeO_6 (X = K, Rb, and Cs). *Int. J. Hydrogen Energy* **2026**, *248*, 155842. [CrossRef]
68. Akter, H.; Hossain, M.M.; Uddin, M.M.; Naqib, S.H.; Ali, M.A. Effects of S substitution on the structural, optoelectronic, and thermomechanical properties of $KTaO_3$ through density functional theory. *J. Phys. Chem. Solids* **2024**, *190*, 112021. [CrossRef]
69. Waqdim, A.; Agouri, M.; Ouali, M.; Abbassi, A.; Taj, S.; Manaut, B.; El Idrissi, M. Ab initio insight into the physical properties of new ferroelectric perovskite oxide materials $XGeO_3$ (X = Sr, Ca). *Rev. Mex. Física* **2024**, *70*. [CrossRef]
70. Gul, B.; Al-Hmoud, M.M.A.; Khan, M.S.; Aziz, S.M. A comparative DFT study of different structures of ZnTe: For optoelectronic and thermoelectric applications. *RSC Adv.* **2025**, *15*, 15550–15560. [CrossRef] [PubMed]
71. Bilal, M.; Shafiq, M.; Ahmad, I.; Khan, I. First principle studies of structural, elastic, electronic and optical properties of Zn-chalcogenides under pressure. *J. Semicond.* **2014**, *35*, 072001. [CrossRef]
72. Mahmood, Q.; Yaseen, M.; Hassan, M.; Ramay, S.M.; Mahmood, A. Theoretical investigation of optical properties and band gap engineering for $Zn_{1-x}TM_xTe$ (TM= Fe, Co) alloys by modified Becke–Johnson potential. *Chin. Phys. B* **2017**, *26*, 087803. [CrossRef]
73. Ziat, Y.; Belkhanchi, H.; Zarhri, Z. DFT Analysis of Structural, Electrical, and Optical Properties of S, Si, and F-Doped GeO_2 Rutile: Implications for UV-Transparent Conductors and Photodetection. *Sol. Energy Sustain. Dev. J.* **2025**, *14*, 74–89. [CrossRef]
74. Bouzaid, A.; Ziat, Y.; Jouad, Y.; Belkhanchi, H. Ab initio analysis of the optoelectronic and photocatalytic properties of codoped $CaZrO_3$ with chalcogen (S, Se, and Te) and titanium (Ti): Influence of pH on band edge positions and CO_2 reduction. *Int. J. Hydrogen Energy* **2026**, *219*, 153991. [CrossRef]
75. Jouad, Y.; Bouzaid, A.; Ziat, Y.; Belkhanchi, H. Boosting the optoelectronic and photocatalytic performance of $KTaO_3$ perovskites with chalcogen (S, Se, and Te) and niobium (Nb) co-doping: A DFT approach. *Chem. Phys.* **2026**, *610*, 113331. [CrossRef]
76. Fox, M. *Optical Properties of Solids*; Oxford University Press: Oxford, UK, 2010; Volume 3.
77. Bouzaid, A.; Ziat, Y.; Belkhanchi, H. Ab initio design of Zr/Te co-doped XTiO3 (X = Ca, Sr) perovskites for enhanced solar-driven hydrogen evolution and optoelectronic energy conversion. *Next Mater.* **2026**, *11*, 101666. [CrossRef]
78. Islam, M.J.; Rabin, M.A.; Gulshan, F. First-principles design of a lead-free $Cs_2LiFeCl_6$ double perovskite for solar-driven hydrogen evolution and CO_2 reduction. *Mater. Adv.* **2026**, *7*, 7037–7052. [CrossRef]

79. Bouzaid, A.; Ziat, Y.; Belkhanchi, H.; Koufi, A.; Jouad, Y. Tuning the optoelectronic and photocatalytic properties of $SrTiO_3$ via S/Zr co-doping: A DFT study. *Next Mater.* **2026**, *12*, 102135. [CrossRef]
80. D'andrea, A.; Del Sole, R. Wannier-mott excitons in semi-infinite crystals: Wave functions and normal-incidence reflectivity. *Phys. Rev. B* **1982**, *25*, 3714. [CrossRef]
81. Fatihi, H.; Ouhenou, H.; Agouri, M.; Benaali, H.; Abbassi, A.; El Idrissi, M.; Manaut, B.; Taj, S. Ba_2VXO_6 (X = Rh, Ir) Double Perovskite Oxides as promising narrow-gap thermoelectrics: Insights from first-principles calculations. *Phys. B Condens. Matter* **2026**, *739*, 418933. [CrossRef]
82. Hisatomi, T.; Kubota, J.; Domen, K. Recent advances in semiconductors for photocatalytic and photoelectrochemical water splitting. *Chem. Soc. Rev.* **2014**, *43*, 7520–7535. [CrossRef] [PubMed]
83. Jang, J.S.; Kim, H.G.; Lee, J.S. Heterojunction Semiconductors: A Strategy to Develop Efficient Photocatalytic Materials for Visible Light Water Splitting. *Catal. Today* **2012**, *185*, 270–277. [CrossRef]
84. Achqraoui, M.; Bekkioui, N.; Jebari, H.; Ez-Zahraouy, H. Exploring layer-dependent photocatalytic and optoelectronic properties of MoS_2 for hydrogen production through DFT analysis. *J. Phys. Chem. Solids* **2025**, *199*, 112543. [CrossRef]
85. Selmi, O.R.; Makhloufi, R.; Charif, R.; Ismael, A.; Taha, T.A.M. First-principles investigation of optoelectronic, thermoelectric, and photocatalytic properties of $Ca_3Zr_{1-x}Sn_xSi_2O_9$. *RSC Adv.* **2026**, *16*, 32972–32989. [CrossRef] [PubMed]
86. Bentour, H.; Boujnah, M.; Houmad, M.; El Yadari, M.; Benyoussef, A.; El Kenz, A. DFT study of Se and Te doped $SrTiO_3$ for enhanced visible-light driven phtocatalytic hydrogen production. *Opt. Quant. Electron* **2021**, *53*, 589. [CrossRef]
87. Bentour, H.; Belasfar, K.; Boujnah, M.; El Yadari, M.; Benyoussef, A.; El Kenz, A. DFT study of Se/Mn and Te/Mn codoped $SrTiO_3$ for visible light-driven photocatlytic hydrogen production. *Opt. Mater.* **2022**, *129*, 112431. [CrossRef]
88. Sharma, G.; Naushad, M.; ALOthman, Z.A.; Iqbal, J.; Bathula, C. High interfacial charge separation in visible-light active Z-scheme g-C_3N_4/MoS_2 heterojunction: Mechanism and degradation of sulfasalazine. *Chemosphere* **2022**, *308*, 136162. [CrossRef] [PubMed]
89. Pearson, R.G. Absolute electronegativity and hardness: Application to inorganic chemistry. *Inorg. Chem.* **1988**, *27*, 734–740. [CrossRef]
90. Mezzat, F.; Zaari, H.; El Kenz, A.; Benyoussef, A. Enhanced visible light photocatalytic activity of $KTaO_3$ (Se, V): DFT investigation. *Comput. Condens. Matter* **2022**, *30*, e00648. [CrossRef]
91. El Goutni, M.E.A.; Ferjani, H.; Batouche, M.; Seddik, T. Spin-orbit coupling driven A_2WCl_6 perovskites: DFT exploration of electronic, optical, and photocatalytic potential for H_2 generation and CO_2 conversion. *J. Phys. Chem. Solids* **2025**, *208*, 113153. [CrossRef]
92. Shinagawa, T.; Takanabe, K. Towards versatile and sustainable hydrogen production through electrocatalytic water splitting: Electrolyte engineering. *ChemSusChem* **2017**, *10*, 1318–1336. [CrossRef] [PubMed]
93. Yang, Z.; Chen, H.; Wu, F.; Hou, Y.; Qiao, J.; Ma, X.; Bai, H.; Ma, B.; Li, J. Investigation on photocatalytic property of SiH/GaSe and SiH/InSe heterojunctions for photocatalytic water splitting. *Int. J. Hydrogen Energy* **2022**, *47*, 31295–31308. [CrossRef]
94. Et-Taleb, A.; Samih, A.; El Fdil, R.; Salmani, E.; Fadil, Z.; Khan, M.N.; Raorane, C.J. Lead-free $LiSiI_3$ perovskite: Bridging photovoltaic efficiency and photocatalytic activity via DFT/SCAPS-1D analysis. *Mater. Today Chem.* **2026**, *55*, 103811. [CrossRef]
95. Lu, Q.; Zhang, B.; Lin, J. Wide-direct-band-gap monolayer carbon nitride CN_2: A potential metal-free photocatalyst for overall water splitting. *RSC Adv.* **2024**, *14*, 24226–24235. [CrossRef] [PubMed]
96. Yang, F.; Boulet, P.; Record, M.-C. DFT Investigation of a Direct Z-Scheme Photocatalyst for Overall Water Splitting: Janus Ga_2SSe/Bi_2O_3 Van Der Waals Heterojunction. *Materials* **2025**, *18*, 1648. [CrossRef] [PubMed]
97. Zhou, P.; Navid, I.A.; Ma, Y.; Xiao, Y.; Wang, P.; Ye, Z.; Zhou, B.; Sun, K.; Mi, Z. Solar-to-hydrogen efficiency of more than 9% in photocatalytic water splitting. *Nature* **2023**, *613*, 66–70. [CrossRef] [PubMed]
98. Das, S.; Parida, V.K.; Tiwary, C.S.; Gupta, A.K.; Chowdhury, S. Emerging contaminants in the aquatic environment: Fate, occurrence, impacts, and toxicity. In *Bioremediation of Emerging Contaminants in Water*; American Chemical Society: Washington, DC, USA, 2024; Volume 1, pp. 1–32. [CrossRef]
99. Adeola, A.O.; Abiodun, B.A.; Adenuga, D.O.; Nomngongo, P.N. Adsorptive and photocatalytic remediation of hazardous organic chemical pollutants in aqueous medium: A review. *J. Contam. Hydrol.* **2022**, *248*, 104019. [CrossRef] [PubMed]
100. Wang, Z.; Cheng, Q.; Wang, X.; Li, J.; Li, W.; Li, Y.; Zhang, G. Carbon dots modified bismuth antimonate for broad spectrum photocatalytic degradation of organic pollutants: Boosted charge separation, DFT calculations and mechanism unveiling. *Chem. Eng. J.* **2021**, *418*, 129460. [CrossRef]
101. Geldasa, F.T.; Kebede, M.A.; Shura, M.W.; Hone, F.G. Experimental and computational study of metal oxide nanoparticles for the photocatalytic degradation of organic pollutants: A review. *RSC Adv.* **2023**, *13*, 18404–18442. [CrossRef] [PubMed]
102. Bissenova, M.; Idrissov, N.; Kuspanov, Z.; Umirzakov, A.; Daulbayev, C. Hybrid adsorption–photocatalysis composites: A sustainable route for efficient water purification. *Mater. Renew. Sustain. Energy* **2025**, *14*, 44. [CrossRef]

103. Ma, Q.; Ming, J.; Sun, X.; Zhang, H.; An, G.; Kawazoe, N.; Chen, G.; Yang, Y. Photocatalytic degradation of multiple-organic-pollutant under visible light by graphene oxide modified composite: Degradation pathway, DFT calculation and mechanism. *J. Environ. Manag.* **2023**, *347*, 119128. [CrossRef] [PubMed]
104. Guzmán, H.; Farkhondehfal, M.A.; Tolod, K.R.; Hernández, S.; Russo, N. Photo/electrocatalytic hydrogen exploitation for CO_2 reduction toward solar fuels production. In *Solar Hydrogen Production*; Academic Press: Cambridge, MA, USA, 2019; pp. 365–418. [CrossRef]
105. Chen, Z.Y.; Huang, N.Y.; Xu, Q. Metal halide perovskite materials in photocatalysis: Design strategies and applications. *Coord. Chem. Rev.* **2023**, *481*, 215031. [CrossRef]
106. Razzaq, A.; In, S.-I. TiO2 Based Nanostructures for Photocatalytic CO_2 Conversion to Valuable Chemicals. *Micromachines* **2019**, *10*, 326. [CrossRef] [PubMed]
107. Zuo, C.; Su, Q.; Yan, X. Research Progress of Co-Catalysts in Photocatalytic CO_2 Reduction: A Review of Developments, Opportunities, and Directions. *Processes* **2023**, *11*, 867. [CrossRef]
108. Cheng, S.; Sun, Z.; Lim, K.H.; Gani, T.Z.H.; Zhang, T.; Wang, Y.; Yin, H.; Liu, K.; Guo, H.; Du, T.; et al. Emerging strategies for CO_2 photoreduction to CH4: From experimental to data-driven design. *Adv. Energy Mater.* **2022**, *12*, 2200389. [CrossRef]
109. Rafiu, R.; Apon, I.A.; Rahman, M.A.; Alsuhaibani, A.M.; Refat, M.S.; Benghanem, M.; AlFaify, S.; Elboughdiri, N. Theoretical investigation of Rb-based double halide perovskites for photovoltaic, photocatalytic water splitting, and CO_2 reduction applications. *RSC Adv.* **2026**, *16*, 30158–30179. [CrossRef] [PubMed]
110. Yu, L.; Zunger, A. Identification of potential photovoltaic absorbers based on first-principles spectroscopic screening of materials. *Phys. Rev. Lett.* **2012**, *108*, 068701. [CrossRef] [PubMed]
111. Shockley, W.; Queisser, H. Detailed balance limit of efficiency of p–n junction solar cells. In *Renewable Energy*; Routledge: Oxfordshire, UK, 2018; Volume 2, pp. 35–54.
112. Rühle, S. Tabulated values of the Shockley–Queisser limit for single junction solar cells. *Sol. Energy* **2016**, *130*, 139–147. [CrossRef]
113. Shahzadi, U.; Bin Javed, M.; Ali, H.T.; Felemban, B.F.; Nazir, S. $Na_2Cu_2TeO_6$: A potential material for high solar cell efficiency and superior energy-harvesting performance. *RSC Adv.* **2026**, *16*, 19079–19093. [CrossRef] [PubMed]

Disclaimer/Publisher's Note: The statements, opinions and data contained in all publications are solely those of the individual author(s) and contributor(s) and not of MDPI and/or the editor(s). MDPI and/or the editor(s) disclaim responsibility for any injury to people or property resulting from any ideas, methods, instructions or products referred to in the content.